electronics

MDPI

Article

Effective Direct Power Control for a Sensor-Less Doubly Fed Induction Generator with a Losses Minimization Criterion

Mahmoud A. Mossa [1,*], Hamdi Echeikh [2], Ahmed A. Zaki Diab [1] and Nguyen Vu Quynh [3,*]

[1] Electrical Engineering Department, Faculty of Engineering, Minia University, Minia 61111, Egypt; a.diab@mu.edu.eg
[2] Department of Electrical Engineering, National Engineering School of Monastir, Monastir 5035, Tunisia; hamdi.engineer.nl@gmail.com
[3] Electrical and Electronics Department, Lac Hong University, Dong Nai 810000, Vietnam
* Correspondence: mahmoud_a_mossa@mu.edu.eg (M.A.M.); vuquynh@lhu.edu.vn (N.V.Q.)

Received: 14 July 2020; Accepted: 4 August 2020; Published: 7 August 2020

check for updates

Abstract: The present paper is concerned with introducing an effective direct power control (DPC) approach for a sensor-less doubly fed induction generator (DFIG). The derivation of the proposed DPC approach is performed in a systematic manner in which the design of the rotor current controllers is well analyzed, which clarifies the real base of the control system as when and why it works properly. The operation of the proposed DPC approach is based on the stator voltage-oriented control principle in which the stator voltage is aligned with the quadrature axis of the rotating reference frame. To obtain maximum generation efficiency, the reactive power reference value is derived based on a loss minimization criterion (LMC) that is described and analyzed in detail. To enhance the robustness of the control system, an effective rotor position estimator is proposed that is robust against the system uncertainties, such as the parameters' variation. To validate the effectiveness of the proposed sensor-less DPC approach, the DFIG dynamic performance is tested for a wide range of operating speeds. The obtained results confirm and emphasize the feasibility of the proposed control approach and its LMC methodology in improving the generation efficiency and in obtaining high dynamic performance from the DFIG.

Keywords: power control; voltage oriented control; losses minimization; sensor-less drive; control design; bode plot; rotor position; co-ordinate transformation

1. Introduction

Recently, generating electricity from wind energy systems has been given great attention due to sustainability, cheapness, economic operation and harvesting capabilities [1,2]. Several research studies have been concerned with introducing robust control techniques for achieving the maximum power extraction from the wind energy systems [3–5]. The corresponding studies used different forms of generation units; some of them have utilized the squirrel-cage-type induction generators (SC IGs) with a capacitor bank connected across the stator terminals to provide the reactive power as reported in [6–8], while the others have utilized the synchronous generators that have stator terminals connected to the grid through a converter as stated in [9–12]. The problems related with these generation units were the disability to operate at variable wind speed, and the difficulty to recover the excessive power to the grid [13,14]. The superiority of the doubly fed induction generator (DFIG) over the other types of wind generators, such as the SC IG, can be clarified through analyzing the mechanism by which the generation unit can handle the power for the variable speed operation. For example, when the SC IG is used, it is required that the rotor speed must be higher than the synchronous speed; but when it is used for large wind turbine systems with large power production, this requires increasing the rotor speed to extra higher values, which make the speed regulation very difficult [15]. The difficulty comes from the fact that the stator terminals of SC IGs are connected directly to the grid through a power converter, and, when handling large power rates, large currents will pass through the power converters, which cannot be afforded by the used converters. At this stage, the DFIG can solve this issue thanks to its physical construction, which enabled it to handle fractions of rated power by managing the frequency of the rotor currents depending on the principle of energy exchange between the stator and rotor sides [16]. This has motivated the researchers to investigate more on the operation analysis of DFIG which became the most widely used generation unit [17–20]. Many advantages have been brought with the DFIG such as the capability of working at variable wind speeds, the ability of controlling the power flow from and to the machine through the rotor terminals, which contributed to reducing the power ratings of the converters to the fractions of rated power, and thus saving the cost and reducing the switching losses as well [21–23].

Some of the introduced control procedures for the DFIG have adopted the vector control concept, in which the reference voltages were calculated using the field oriented control (FOC) or the direct torque control (DTC) techniques [24–27]. The FOC control has suffered from the system complexity due to the need for performing several co-ordinates transformation. Moreover, in several cases, the proper design of proportional-integral (PI) current regulators was not ensured which resulted in deteriorating the transient response of the system [28,29]. Some attempts have been carried out to make the selection of the PI gains more precise as in [30,31], which used the neural and fuzzy systems to optimally select the gains. However, good results have been obtained, but the system complexity is increased; this is besides adding a delay in the system response. The DTC technique solved the complexity issue via utilizing two hysteresis regulators for the torque and the flux instead of incorporating the PI regulators [32–34]. However, the main issue of the DTC was the remarkable torque and current oscillations due to the imprecise selection of voltage vectors [35]. The imprecise voltage selection under the DTC can be referred to the mechanism by which the DTC works, as when a voltage vector is selected from the look-up table, it will be applied for the entire sampling interval, and during this interval it may happens that the torque or flux error decreases, which means that the applied vector is no longer valid in this situation and thus it can result in increasing the torque or flux deviation, which finally increases the ripples. The most significant control topology, which has been tested with the DFIG based on the vector control principle, was the direct power control (DPC) in which the generated active and reactive powers were controlled by regulating the direct (d) and quadrature (q) axes components of the rotor current [36–39]. This technique has contributed in well understanding the DFIG dynamic behavior and in obtaining high dynamic performance from the drive. However, most of the introduced DPC control techniques did not introduce a detailed investigation about the core principle based upon which the current controllers have been designed, which made it difficult to understand the base operation of the DPC. For example, investigating the inherent coupling between the d-axis and q-axis component of the controlled variables (rotor voltages and currents) has not been properly handled. Based upon this, the current paper presents a detailed analysis for the derivation of the vector control system through which the coupling analysis and its restricting mechanism are introduced and analyzed.

Improving the DFIG efficiency has not been given a sufficient concern from the previous studies; this has been noticed in several studies in which the control system was designed considering a constant zero value of reactive power reference to realize a unity power factor during the operation. To avoid this deficiency, the current paper introduces an effective losses minimization criterion (LMC) through which the DFIG losses can be minimized and the efficiency can be consequently improved. In the proposed LMC, the reactive power reference value is derived via utilizing the value of the d-axis component of stator current, which achieves minimum losses (copper and iron) for the DFIG.

Another important aspect about the DFIG is the realization of a sensor-less operation to increase the reliability of the system. Many sensor-less control procedures have been introduced for the

DFIG [40–43], some of which have utilized the model reference adaptive system (MRAS) observers that extract the speed information and the rotor position through comparing two values of the estimated rotor flux [40,41]. The main issue of these techniques was the dependency on the machine parameters, mainly the stator resistance, which is subjected to variation under different operating conditions. A lot of attempts were made to increase the robustness of the estimator against the parameters' variations (mainly the stator resistance), but this has resulted in increasing the system complexity via adding extra computation parts to the system [42,43]. In [44,45], the extended kalman filter has been introduced for estimating the speed and rotor position for the DFIG. The problem with the kalman filter was that it considered the linear models of the system and observer, which was not so precise especially when applied with highly non-linear system such as the DFIG; adding to this, was the complexity of the system. Another study has proposed an estimator in which the rotor position was obtained through estimating the rotor current in two different frames (stationary and rotor) [46–48]. The main problem with this estimator was the dependency on the machine parameters (mainly stator resistance) when estimating the rotor current position in stationary frame.

For this purpose, the current paper introduces a robust rotor position estimator, which extracts the rotor position with minimal dependency on the machine parameters to achieve precise co-ordinate transformation.

The contributions of the paper are summarized as follows:

1. A new design procedure for the direct power control of the DFIG has been introduced.
2. The new control design has been described and analyzed in a systematic manner, which enables understanding the control dynamics: when and why it works properly.
3. An effective losses minimization criterion (LMC) has been formulated in order to improve the DFIG efficiency. The derivation of the LMC has been described in detail.
4. A robust rotor position estimator has been designed and tested for various operating speeds. The proposed estimator is simple in construction and non-sensitive to the machine parameters' variation.
5. Extensive tests are carried out to validate the proposed DPC control system and the LMC with the position estimator. The obtained results confirm the feasibility of the system and its ability to achieve the desired dynamic performance with high precision.

The paper starts by introducing the mathematical model and the equivalent circuit of the DFIG, and then the proposed DPC and the design of the rotor current controllers are described in detail. After that, the proposed losses minimization criterion (LMC) is introduced and analyzed. Finally, the proposed sensor-less position estimator is introduced and described and then the testing results and conclusion are presented.

2. Proposed DPC Approach

2.1. Design of Rotor Current Controllers

In order to construct the proposed DPC and design the current controllers, a mathematical model for the DFIG defined in a reference frame rotating with the synchronous angular speed of stator voltage is presented. The mathematical model is derived using the circuit shown in Figure 1.

In Figure 1, the superscript 'sv' refer to the stator voltage frame in which the stator voltage vector is aligned with the q-axis of the rotating reference frame. The parameters R_s and R_r denote to the stator and rotor resistances, while the parameters L_m, L_{ls} and L_{lr} denote to the magnetizing, leakage stator and leakage rotor inductances, respectively. The variables $\bar{i}_s^{sv}$ and $\bar{i}_r^{sv}$ refer to the stator and rotor currents defined in the synchronous frame, while $\overline{\psi}_s^{sv}$ and $\overline{\psi}_r^{sv}$ refer to the stator and rotor fluxes. The angular speeds $\omega_{\overline{u}_s}$ and ω_{me} refer to synchronous and mechanical angular speeds, respectively. The voltage vectors $\overline{u}_s^{sv}$ and $\overline{u}_r^{sv}$ refer to the stator and rotor voltages defined in the rotating frame.

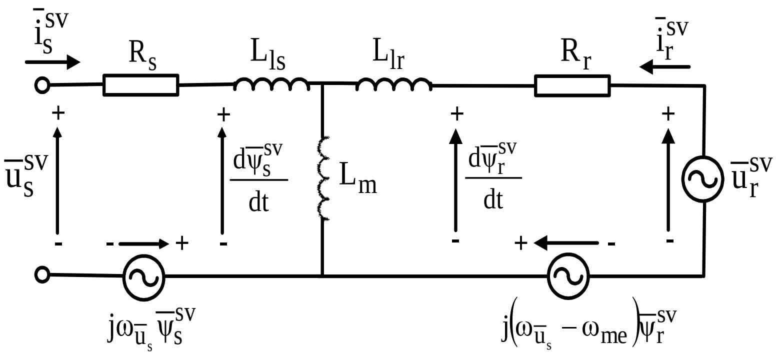

Figure 1. Equivalent circuit of a doubly fed induction generator (DFIG) in a synchronous reference frame.

The voltage balance in the circuit of Figure 1 can be expressed by:

$$\bar{u}_s^{sv} = R_s \bar{i}_s^{sv} + \frac{d\bar{\psi}_s^{sv}}{dt} + j\omega_{\bar{u}_s}\bar{\psi}_s^{sv} \tag{1}$$

$$\bar{u}_r^{sv} = R_r \bar{i}_r^{sv} + \frac{d\bar{\psi}_r^{sv}}{dt} + j\left(\omega_{\bar{u}_s} - \omega_{me}\right)\bar{\psi}_r^{sv} \tag{2}$$

The vectors' allocation in different reference frames can be shown in Figure 2. Form this figure, it can be noticed that the stator voltage vector $\bar{u}_s^{sv}$ is aligned with q-axis of the rotating reference frame (rotates with $\omega_{\bar{u}_s}$) and thus the stator flux supposed to be lagged with angle of 90° behind the stator voltage. Moreover, it can be noticed that the rotor current vector $\bar{i}_r^{sv}$ makes an angle of $\theta^s_{\bar{i}_r}$ with the d^s-axis of stationary frame, while it makes an angle of $\theta^r_{\bar{i}_r}$ with the d^r-axis of the rotor reference frame. Thus, it can be deduced that the difference between the two positions of the rotor current vectors gives the rotor position $\theta_{me} = \theta^s_{\bar{i}_r} - \theta^r_{\bar{i}_r}$, as will be explained later.

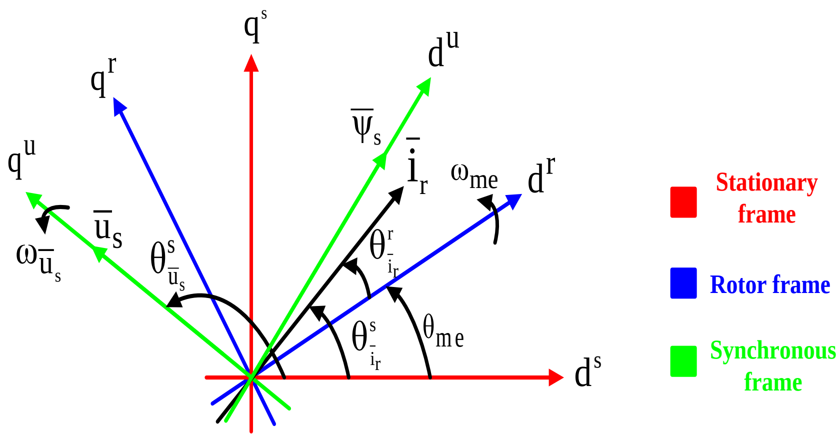

Figure 2. Spatial distribution of the vectors in different reference frames.

With the help of Figure 2, and under stator voltage oriented (SVO) control, the following relationships are obtained under steady-state operating conditions:

$$u_{qs}^{sv} = \left|\bar{u}_s^{sv}\right|, \text{ and } u_{ds}^{sv} = 0.0 \tag{3}$$

$$\psi_{ds}^{sv} \cong \left|\bar{\psi}_s^{sv}\right|, \text{ and } \psi_{qs}^{sv} \cong 0.0 \tag{4}$$

where u_{ds}^{sv} and u_{qs}^{sv} are the d-q components of stator voltage vector. Meanwhile, ψ_{ds}^{sv} and ψ_{qs}^{sv} are the d-q components of the stator flux vector, all defined in a synchronous frame.

Then, the generated active (P_s) and reactive power (Q_s) can be also evaluated under SVO control using (3) and (4) by

$$P_s = 1.5u_{qs}^{sv}i_{qs}^{sv},\ \text{and}\ Q_s = 1.5u_{qs}^{sv}i_{ds}^{sv} \tag{5}$$

where i_{ds}^{sv} and i_{qs}^{sv} are the d-q components of stator current vector represented in the rotating frame.

Using the flux–current relationships, the active and reactive powers can be expressed in terms of rotor current components as follows

$$P_s = -1.5\frac{L_m}{L_s}u_{qs}^{sv}i_{qr}^{sv},\ \text{and}\ Q_s = 1.5\frac{L_m}{L_s}u_{qs}^{sv}\left(\frac{u_{qs}^{sv}}{L_m\omega_{u_s}} - i_{dr}^{sv}\right) \tag{6}$$

where i_{dr}^{sv} and i_{qr}^{sv} are the d-q components of rotor current vector expressed in the rotating frame.

From (6), it can be realized that the active and reactive powers of the DFIG can be controlled via regulating the quadrature and direct axes components of rotor current (i_{dr}^{sv} and i_{qr}^{sv}), respectively. Upon this hypothesis, the design of rotor current controllers is derived and analyzed as follows:

From (1) and (2), and by taking the Laplace transform, it results:

$$\overline{U}_s^{sv}(s) = \left(R_s + sL_s + j\omega_{\overline{u}_s}L_s\right)\overline{I}_s^{sv}(s) + \left(sL_m + j\omega_{\overline{u}_s}L_m\right)\overline{I}_r^{sv}(s) \tag{7}$$

$$\overline{U}_r^{sv}(s) = \left(R_r + sL_r + j\left(\omega_{\overline{u}_s} - \omega_{me}\right)L_r\right)\overline{I}_r^{sv}(s) + \left(sL_m + j\left(\omega_{\overline{u}_s} - \omega_{me}\right)L_m\right)\overline{I}_s^{sv}(s) \tag{8}$$

where s refers to the Laplace domain.

From (7) and (8) and after some mathematical derivations, the rotor current can be expressed by:

$$\overline{I}_r^{sv}(s) = \frac{\overline{U}_r^{sv}(s) * \left(R_s + \left(S + j\omega_{\overline{u}_s}\right)L_s\right) - \left(S + j\left(\omega_{\overline{u}_s} - \omega_{me}\right)\right)L_m * \left(\overline{U}_s^{sv}(s) - \left(S + j\omega_{\overline{u}_s}\right)L_m\overline{I}_r^{sv}(s)\right)}{\left(R_s + \left(S + j\omega_{\overline{u}_s}\right)L_s\right) * \left(R_r + \left(S + j\left(\omega_{\overline{u}_s} - \omega_{me}\right)\right)L_r\right)} \tag{9}$$

Via utilizing (9), the transfer function $\left(\frac{\overline{I}_r^{sv}(s)}{\overline{U}_r^{sv}(s)}\right)$ can be derived to show the effect of rotor current variation respecting to the applied rotor voltage, while the response of $\overline{I}_r^{sv}(s)$ respecting to the stator voltage $\overline{U}_s^{sv}(s)$ is considered as a disturbance, which, at this stage, can be neglected, then the transfer function $\left(\frac{\overline{I}_r^{sv}(s)}{\overline{U}_r^{sv}(s)}\right)$ can be expressed by:

$$\frac{\overline{I}_r^{sv}(s)}{\overline{U}_r^{sv}(s)} = \frac{R_s + \left(S + j\omega_{\overline{u}_s}\right)L_s}{\left(R_s + \left(S + j\omega_{\overline{u}_s}\right)L_s\right) * \left(R_r + \left(S + j\left(\omega_{\overline{u}_s} - \omega_{me}\right)\right)L_r\right) - \left(S + j\left(\omega_{\overline{u}_s} - \omega_{me}\right)\right) * \left(S + j\omega_{\overline{u}_s}\right)L_m^2} \tag{10}$$

Assuming that the rotor is rotating with an angular speed of $\omega_{me} = \omega_{\overline{u}_s}$, then the slip will be zero and this will simplify (10) to derive the poles and zeros of the transfer function as follows:

$$\frac{\overline{I}_r^{sv}(s)}{\overline{U}_r^{sv}(s)} = \frac{Num(S)}{Den(S)} = \frac{R_s + \left(S + j\omega_{\overline{u}_s}\right)L_s}{S^2\left(L_sL_r - L_m^2\right) + S\left[R_sL_r + R_rL_s + j\omega_{\overline{u}_s}\left(L_sL_r - L_m^2\right)\right] + \left(R_s + j\omega_{\overline{u}_s}L_s\right)R_r} \tag{11}$$

From (11), it can be realized that the denominator has complex coefficients, which means that the real axis component of the applied input vector (which is here u_{dr}^{sv}) affects both components of the outputs (i_{dr}^{sv} and i_{qr}^{sv}) and the same is applied to the imaginary part of the applied input vector (u_{qr}^{sv}). This behavior therefore indicates the presence of cross-coupling between the two axes (d and q) of the reference system and this fact has to be taken into consideration while designing the current regulators.

By substituting the DFIG parameters values into (11), and after analyzing the roots of the nominator and denominator, the zeros (Z) and poles (P_1,P_2) of the transfer function can be determined and then the transfer function can be represented by:

$$\frac{\overline{I}_r^{sv}(s)}{\overline{U}_r^{sv}(s)} = \frac{1-\frac{S}{Z}}{R_r\left(1-\frac{S}{P_1}\right)\left(1-\frac{S}{P_2}\right)} \tag{12}$$

The transfer function (11) outlines the characteristics of the rotor current regulators and can be represented using the block diagram in Figure 3, in which R(s) denotes to the current regulator and $I_r^*(S)$ is the reference rotor current.

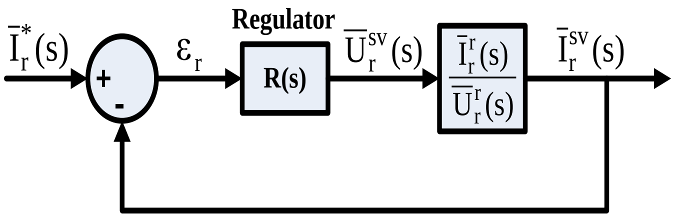

Figure 3. Schematic of rotor current controller.

To avoid the coupling issue, a possible choice for the regulator R(s) is to carry out pole-zero and zero-pole cancellations with the transfer function $\left(\frac{\overline{I}_r^{sv}(s)}{\overline{U}_r^{sv}(s)}\right)$ and placing a pole in the origin so as to realize the fundamental condition of having zero error. In other words, a proportional integrator-derivative (PID)-type regulator is created using the following expression:

$$R(S) = \frac{K}{S}\frac{\left(1-\frac{S}{P_1}\right)\left(1-\frac{S}{P_2}\right)}{\left(1-\frac{S}{Z}\right)} \tag{13}$$

The pole-zero deletion eliminate the cross coupling between the two axes, and thus the block diagram in Figure 3 will be reconfigured to be as in Figure 4 in which the factor $K' = \frac{K}{R_r}$ and K is the gain of the proportional part.

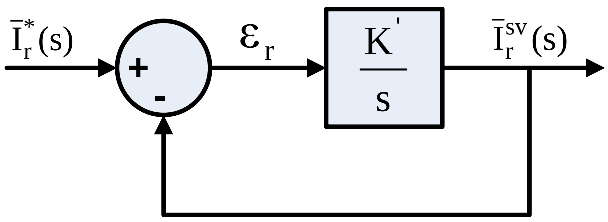

Figure 4. Simplified form of rotor current controller.

From Figure 4, it is possible to write the two components of the rotor current vector $\overline{I}_r^{sv}(s)$ as follows:

$$I_{dr}^{sv}(S) + jI_{qr}^{sv}(S) = \frac{K'}{S}\left(\varepsilon_{dr} + j\varepsilon_{qr}\right) \tag{14}$$

From (14), it can be realized that each current component depends only on the error relating to its own axis (ε_{dr} and ε_{qr}) and not on both of them, and this is achieved only if a perfect decoupling is ensured through the proper choice of the gain K.

To achieve the perfect decoupling, the regulator R(s) has to be represented in a scalar form so that it can be possible to derive the d-q components of the reference output through which the decoupling can be checked. This action can be realized via substituting the values of Z, P_1 and P_2 with their real parameters given in Appendix A into (13), then it results:

$$R(S) = \frac{A+jB}{Den} = \frac{K}{S}\left[\frac{6.366e^{-8}s^3 + 1.86e^{-5}s^2 + \left(6.399e^{-3} - j2.49e^{-6}\right)s + 1}{1.014e^{-5}s^2 + 8.74e^{-5}s + 1}\right] \tag{15}$$

By utilizing (15), the d-q components of the rotor voltage vector (output of the current controller) can be calculated as follows:

$$\overline{U}_r^{sv}(s) = U_{dr}^{sv}(s) + jU_{qr}^{sv}(s) = R(S) * \left(\varepsilon_{dr} + j\varepsilon_{qr}\right) = \frac{K}{S} * \frac{A + jB}{Den} * \left(\varepsilon_{dr} + j\varepsilon_{qr}\right) \quad (16)$$

By separating the d-q components in (16), it results:

$$U_{dr}^{sv}(s) = \frac{K}{S * Den}\left(A\varepsilon_{dr} - B\varepsilon_{qr}\right), \text{ and } U_{qr}^{sv}(s) = \frac{K}{S * Den}\left(A\varepsilon_{qr} + B\varepsilon_{dr}\right) \quad (17)$$

From (17), it is clear that there is a coupling between the two components of rotor voltage vector and here the role of the gain K comes into consideration. As the DFIG is connected to a wind turbine system, so it is sufficient for the control to be able to follow the wind variations which supposed to be relatively slow and therefore it is suitable to select a band-pass frequency of 10–15 Hz for the current loops, which, after calculation, gives a value of K equals 10.

Figure 5 confirms the validity of the selected value of K, as it can be seen that the two current loops (represented by their d and q components) are stable with phase margin of 90° for three different values of K. So, it can be concluded that the precise decoupling is achieved.

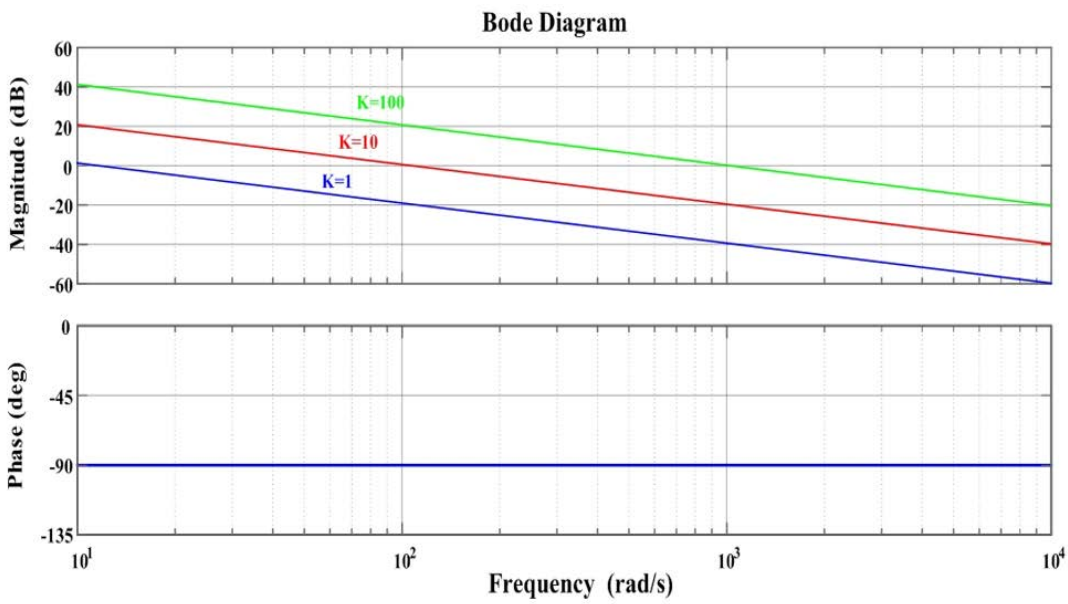

Figure 5. Bode plot of transfer function R(s) for different K gain values.

In conclusion of the design procedure, the schematic diagram of the rotor current regulators can be constructed as shown in Figure 6 via utilizing the relationships (16) and (17). The important role that the term $\frac{B'}{Den}$ plays in limiting the coupling between the two axes is very clear, and this can be investigated through the results shown in Figure 6 in which a comparison is made between the response of the rotor current components to their references with and without incorporating the term $\frac{B'}{Den}$ into the control scheme. In Figure 6a, in which the term $\frac{B'}{Den}$ is incorporated, the decoupling is achieved between the d-q components, while, in Figure 6b, with removing the term $\frac{B'}{Den'}$ a noticeable coupling is exist between the two axes. The constant B′ refers to $B' = \frac{B}{S}$.

Moreover, in order to have a perfect decoupling, the estimation of rotor position θ_{me} has to be precise, as the co-ordinates' transformation requires the rotor position information. For this reason, a robust position estimator is presented and described in Section 3.

The references $\left(I_{dr}^*\right)^{sv}$ and $\left(I_{qr}^*\right)^{sv}$ are obtained using (6) in which the references active and reactive powers are utilized. The active power reference value P_s^* is directly imposed according to the generation requirements, while the reactive power reference is applied based on a certain criterion, which is the minimization of DFIG losses (copper+ iron), as described in the following subsection.

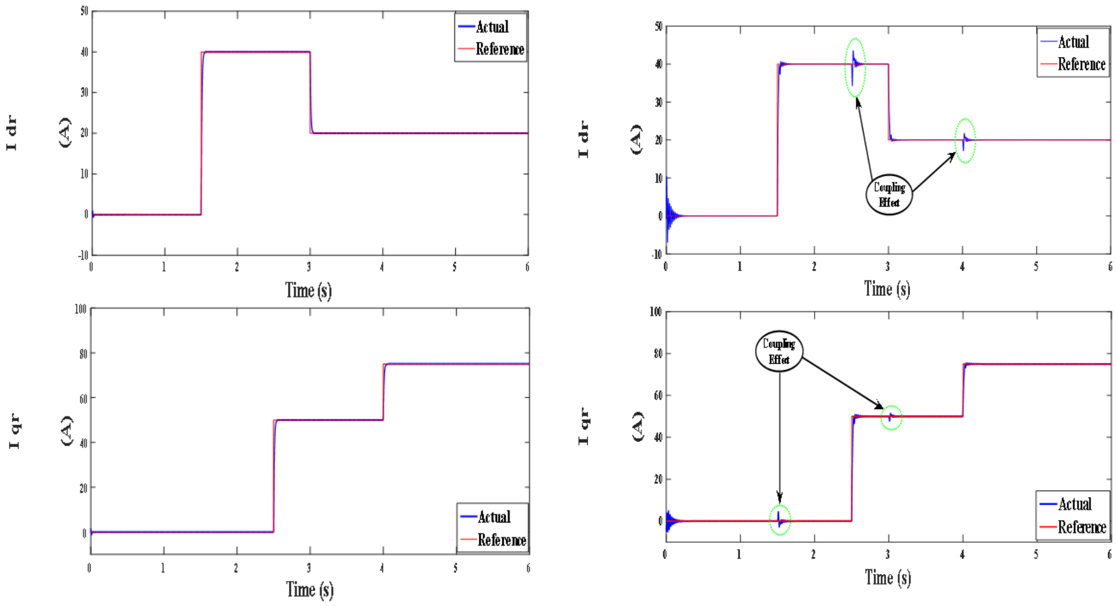

(**a**) (**b**)

Figure 6. Rotor current dynamics using the proposed current controllers. (**a**) Rotor current response with the term $\frac{B'}{Den}$; (**b**) rotor current response with the term $\frac{B'}{Den}$ excluded.

2.2. Losses Minimization Criterion

To calculate the losses (copper and iron) of DFIG, the iron loss has to be considered when modeling the DFIG. The magnetizing branch of the DFIG model when taking the iron loss into consideration can be represented as shown in Figure 7.

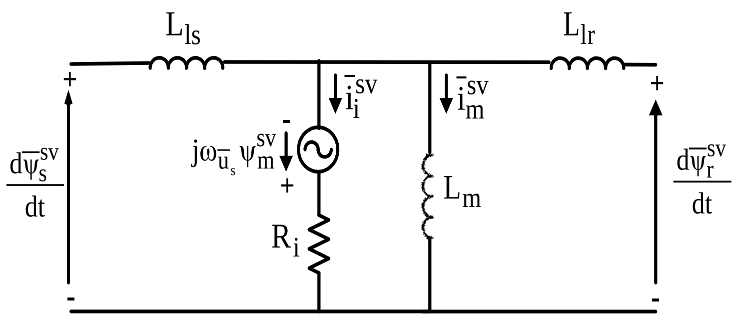

Figure 7. Magnetization branch considering iron losses under SVOC.

The relationships that outline the dynamics in the magnetizing branch of Figure 7 are expressed by:

$$\omega_{\bar{u}_s}\psi_{qm}^{sv} = -R_i i_{di}^{sv} + \frac{d\psi_{dm}^{sv}}{dt} \tag{18}$$

$$\omega_{\bar{u}_s}\psi_{dm}^{sv} = R_i i_{qi}^{sv} - \frac{d\psi_{qm}^{sv}}{dt} \tag{19}$$

where $\bar{i}_m^{sv}$ is the magnetizing current and $\bar{i}_i^{sv}$ is the iron branch current and $\overline{\psi}_m^{sv}$ is the magnetizing flux and R_i is the iron resistance.

Under normal grid conditions, the variation in the magnetizing flux can be ignored, and the relationships (18) and (19) tend to be:

$$\omega_{\overline{u}_s}\psi_{qm}^{sv} = -R_i i_{di}^{sv}, \text{ and } \omega_{\overline{u}_s}\psi_{dm}^{sv} = R_i i_{qi}^{sv} \tag{20}$$

Moreover, under SVO control, the following relationships are obtained:

$$\psi_{qs}^{sv} = 0.0 = \psi_{qm}^{sv} + L_{ls} i_{qs}^{sv} \tag{21}$$

$$\psi_{ds}^{sv} = \psi_{dm}^{sv} + L_{ls} i_{ds}^{sv} \tag{22}$$

By substituting from (21) and (22) into (20), the d-q components of the current in the iron branch are calculated by:

$$i_{di}^{sv} = \frac{\omega_{\overline{u}_s}}{R_i} L_{ls} i_{qs}^{sv}, \text{ and } i_{qi}^{sv} = \frac{\omega_{\overline{u}_s}}{R_i}\left(\psi_{ds}^{sv} - L_{ls} i_{ds}^{sv}\right) \tag{23}$$

The iron losses (P_{losses}^{ir}) for the DFIG can be calculated using the iron loss current components as applied for the IM in [49], and extended here to the DFIG as follows:

$$P_{losses}^{ir} = 1.5R_i\left(\left(i_{di}^{sv}\right)^2 + \left(i_{qi}^{sv}\right)^2\right) \tag{24}$$

Moreover, under SVO control, the developed electromagnetic torque of the DFIG can be expressed by:

$$T_e = 1.5p\psi_{ds}^{sv} i_{qs}^{sv} \tag{25}$$

where p is the pole pairs. Then, via utilizing (23) and (25) and by substituting in (24), the iron losses yields to:

$$P_{losses}^{ir} = 1.5\frac{\omega_{\overline{u}_s}^2}{R_i}\left[\frac{L_{ls}^2}{(1.5p)^2}\left(\frac{T_e}{\psi_{ds}^{sv}}\right)^2 + \psi_{ds}^{sv\,2} - 2L_{ls} i_{ds}^{sv}\psi_{ds}^{sv} + L_{ls}^2 i_{ds}^{sv\,2}\right] \tag{26}$$

The second type of losses is the copper losses (P_{losses}^{cu}), which can be evaluated by:

$$P_{losses}^{cu} = 1.5R_s\left(\left(i_{ds}^{sv}\right)^2 + \left(i_{qs}^{sv}\right)^2\right) + 1.5R_r\left(\left(i_{dr}^{sv}\right)^2 + \left(i_{qr}^{sv}\right)^2\right) \tag{27}$$

Through utilizing the currents–fluxes relationships under SVO control, (27) tends to be:

$$P_{losses}^{cu} = 1.5\left[i_{ds}^{sv\,2}\left(R_s + \left(\frac{L_s}{L_m}\right)^2 R_r\right) - 2\frac{L_s R_r}{L_m^2}\psi_{ds}^{sv} i_{ds}^{sv} + \frac{1}{(1.5p)^2}\left(\frac{T_e}{\psi_{ds}^{sv}}\right)^2\left(R_s + \left(\frac{L_s}{L_m}\right)^2\right) + \left(\frac{\psi_{ds}^{sv}}{L_m}\right)^2 R_r\right] \tag{28}$$

Until now, the total losses can be evaluated by adding (26) to (28), which results in:

$$P_{losses}^{total} = P_{losses}^{ir} + P_{losses}^{cu} \tag{29}$$

From (29), it can be concluded that the total losses can be evaluated using the d-axis component of stator current i_{ds}^{sv} in case of normal grid conditions under which the stator flux ψ_{ds}^{sv} is assumed to be constant. Thus, by differentiating (29) with respect to i_{ds}^{sv} and equalizing the result to zero, the optimal current value $i_{ds}^{sv,opt}$, which achieves minimum losses, can be obtained by:

$$i_{ds}^{sv,opt} = \frac{\left(L_{ls}L_m^2\omega_{\overline{u}_s}^2 + R_r R_i L_s\right)\psi_{ds}^{sv}}{\left(L_{ls}L_m^2\omega_{\overline{u}_s}^2 + R_s R_i L_m^2 + R_r R_i L_s^2\right)} \tag{30}$$

Now, by utilizing (30) and substituting in (5), the optimal reactive power reference $Q_s^{*,opt}$, which achieves minimum losses, can be expressed by:

$$Q_s^{*,opt} = 1.5 u_{qs}^{sv} i_{ds}^{sv,opt} \tag{31}$$

Until now, the rotor current references to be utilized by the DPC system shown in Figure 8 can be calculated by:

$$i_{dr}^{sv,*} = \frac{u_{qs}^{sv}}{L_m \omega_{\overline{u}_s}} - \frac{Q_s^{*,opt}}{1.5(L_m/L_s) u_{qs}^{sv}} \tag{32}$$

$$i_{qr}^{sv,*} = \frac{-P_s^*}{1.5(L_m/L_s) u_{qs}^{sv}} \tag{33}$$

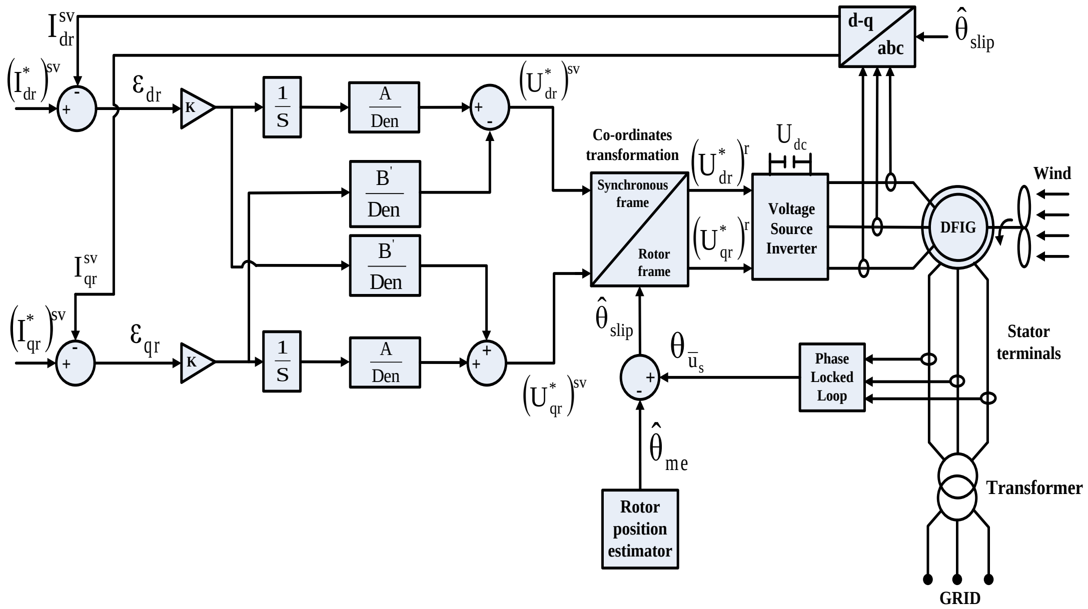

Figure 8. Configuration of rotor current controllers for a DFIG.

The last important part in the control scheme is the rotor position estimator, which is described in the following section.

3. Estimation of Rotor Position

As can be noticed from Figure 8, the precise estimation of rotor position is mandatory; this is to ensure the correct transformation between different reference frames (mainly between the rotor and synchronous frames). The proposed rotor position estimator is designed ensuring the minimum dependency on the machine parameters while keeping the system as simple as possible. The proposed position estimator avoids the direct integration of stator flux in order to overcome the integration and DC drift problems.

The proposed estimator utilizes Figure 2, which illustrates the space displacements between different vectors. For example, the rotor current vector has an angular displacement of $\theta_{\bar{i}_r}^s$ with the direct axis of stator frame; meanwhile, it has an angular displacement of $\theta_{\bar{i}_r}^r$ with the direct axis of rotor frame. The difference between the two displacments ($\theta_{\bar{i}_r}^s$ and $\theta_{\bar{i}_r}^r$) formulates the rotor position according to the following relationship

$$\hat{\theta}_{me} = \theta_{\bar{i}_r}^s - \theta_{\bar{i}_r}^r \tag{34}$$

For the DFIG, both stator and rotor currents can be measured directly each in their relative frames, but the rotor current and its position $\theta^s_{\bar{i}_r}$ cannot be measured in the stator frame, and thus they must be estimated.

The rotor current vector $\bar{i}^s_r$ can be estimated in the stator frame by:

$$\bar{i}^s_r = \frac{1}{L_m}\left(\overline{\psi}^s_s - L_s \bar{i}^s_s\right) \tag{35}$$

In addition, the magnetizing current can be estimated in the stator frame by:

$$\bar{i}^s_m = \frac{\overline{\psi}^s_s}{L_m} = (1+\sigma_s)\bar{i}^s_s + \bar{i}^s_r \tag{36}$$

where $\sigma_s = \frac{L_s}{L_m} - 1$, is the leakage factor of stator.

By representing (1) in stator frame ($\omega_{\overline{u}_s} = 0$), it results:

$$\overline{u}^s_s = R_s \bar{i}^s_s + \frac{d\overline{\psi}^s_s}{dt} \tag{37}$$

The stator resistance R_s and its voltage drop can be neglected, and thus a displacement angle of 90° is formulated between the stator voltage ($\overline{u}^s_s$) and stator flux ($\overline{\psi}^s_s$) vectors.

From Figure 2, it can be realized that the current vector $\bar{i}^s_m$ and flux vector $\overline{\psi}^s_s$ have a displacement angle of $\left(\theta^s_{\overline{u}_s} - 90\right)$ with respect to the direct axis of stator the frame. Then, by utilizing (36), the d^s-q^s components of the current vector $\bar{i}^s_m$ can be calculated by:

$$i^s_{md} = \left|\bar{i}^s_m\right| \cos\left(\theta^s_{\overline{u}_s} - 90\right) = \left|\bar{i}^s_m\right| \sin\theta^s_{\overline{u}_s} \tag{38}$$

$$i^s_{mq} = \left|\bar{i}^s_m\right| \sin\left(\theta^s_{\overline{u}_s} - 90\right) = -\left|\bar{i}^s_m\right| \cos\theta^s_{\overline{u}_s} \tag{39}$$

Using (38) and (39), the d^s-q^s components of rotor current vector can be obtained as follows:

$$i^s_{dr} = i^s_{md} - (1+\sigma_s)i^s_{ds}, \text{ and } i^s_{qr} = i^s_{mq} - (1+\sigma_s)i^s_{qs} \tag{40}$$

$$, \text{ and } \left|\bar{i}^s_r\right| = \sqrt{\left(i^s_{dr}\right)^2 + \left(i^s_{qr}\right)^2} \tag{41}$$

Using (40) and (41), the unit vectors of rotor current position $\theta^s_{\bar{i}_r}$ expressed in stationary frame can be calculated by:

$$\cos\theta^s_{\bar{i}_r} = \frac{i^s_{dr}}{\left|\bar{i}^s_r\right|}, \text{ and } \sin\theta^s_{\bar{i}_r} = \frac{i^s_{qr}}{\left|\bar{i}^s_r\right|} \tag{42}$$

Alternatively, the unit vectors of rotor current position $\theta^r_{\bar{i}_r}$ defined in the rotor frame can be evaluated by:

$$\cos\theta^r_{\bar{i}_r} = \frac{i^r_{dr}}{\left|\bar{i}^r_r\right|}, \text{ and } \sin\theta^r_{\bar{i}_r} = \frac{i^r_{qr}}{\left|\bar{i}^r_r\right|} \tag{43}$$

Now, by applying (42) and (43), the unit vectors of the rotor position $\hat{\theta}_{me}$ can be calculated as follows:

$$\sin\hat{\theta}_{me} = \sin\left(\theta^s_{\bar{i}_r} - \theta^r_{\bar{i}_r}\right) = \sin\theta^s_{\bar{i}_r}\cos\theta^r_{\bar{i}_r} - \sin\theta^r_{\bar{i}_r}\cos\theta^s_{\bar{i}_r} \tag{44}$$

$$\cos\hat{\theta}_{me} = \cos\left(\theta^s_{\bar{i}_r} - \theta^r_{\bar{i}_r}\right) = \cos\theta^s_{\bar{i}_r}\cos\theta^r_{\bar{i}_r} + \sin\theta^s_{\bar{i}_r}\sin\theta^r_{\bar{i}_r} \tag{45}$$

The relationships (44) and (45) report that the estimation accuracy is mainly depended on the magnetizing current $\left|\bar{i}_m^s\right|$ as all other variables can be directly measured. The estimated value of $\bar{i}_m^s$ is obtained using (36), and thus the current $\bar{i}_m^s$ is calculated in terms of the flux vector $\overline{\psi}_s^s$, which is estimated using the voltage model of the machine through integration.

The sensitivity of stator voltage to the noise is very high in case that no precautions are taken during the measurement. The accompanied noise will be magnified if the pure integration is applied, and finally the estimated flux quality is deteriorated. In addition, to avoid any saturation problem, the value of L_m must be accurately acknowledged. This requires the use of an online adaptation mechanism of L_m, which inreases the complexity of the control system.

To avoid the dependency on L_m and the voltage integration problems, a re-computation mechanism is used to estimate $\left|\bar{i}_m^s\right|$. In this technique, it is assumed that the variations of stator flux and magnetizing current vectors are very slow with respect to the sampling time (T_s).

The re-computation process is formulated by discretizing the control cycles into sampling periods kT_s, $(k+1)T_s$, $(k+2)T_s$, ... , so that $\left|\bar{i}_m^s\right|$ can be calculated at kT_s using the sampled quantities at the anticipated interval $(k-1)T_s$ as follows:

$$i_{dr,k}^{s'} = i_{dr,k}^{r} \cos\hat{\theta}_{me,k-1} - i_{qr,k}^{r} \sin\hat{\theta}_{me,k-1} \tag{46}$$

$$i_{qr,k}^{s'} = i_{qr,k}^{r} \cos\hat{\theta}_{me,k-1} + i_{dr,k}^{r} \sin\hat{\theta}_{me,k-1} \tag{47}$$

Using (46) and (47), the d-q components of $\bar{i}_m^s$ can be evaluated at instant kT_s by:

$$i_{md,k}^{s'} = \frac{L_s}{L_m} i_{ds}^{s} + i_{dr,k}^{s'}, \text{ and } i_{mq,k}^{s'} = \frac{L_s}{L_m} i_{qs}^{s} + i_{qr,k}^{s'} \tag{48}$$

Then, the current $\left|i_{m,k}^{s'}\right|$ can be calculated by:

$$\left|i_{m,k}^{s'}\right| = \sqrt{\left(i_{md,k}^{s'}\right)^2 + \left(i_{mq,k}^{s'}\right)^2} \tag{49}$$

A low pass filter is then used to smooth any expected error in the values that are calculated at instant $(k-1)T_s$ using (48).

By substituting from (49) into (38) and (39), and following the calculation procedure from (41) to (45), the rotor position $\hat{\theta}_{me}$ can be evaluated. The layout of the rotor position estimator is shown in Figure 9 which summarizes the steps from (34) to (49).

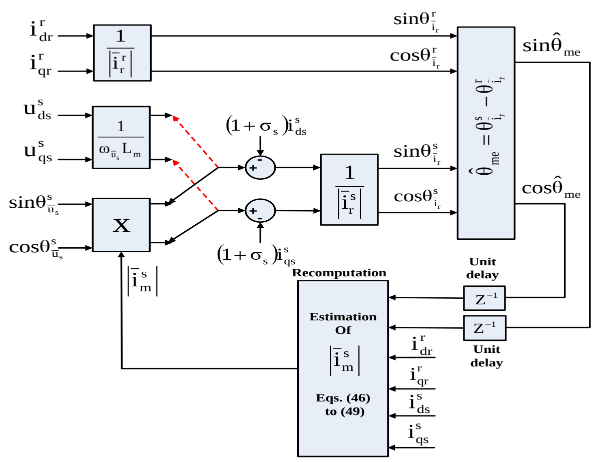

Figure 9. Proposed rotor position estimator.

As the control starts in flight, it is difficult to assign an initial value of $\hat{\theta}_{me}$. Despite that, the initial value of $\left|\bar{i}_m^s\right|$ can be easy applied. This is remarked with dashed red lines in Figure 9. The initial value of $\left|\bar{i}_m^s\right|$ is obtained using the following expression:

$$\left|\bar{i}_m^s\right| = \frac{\left|\bar{u}_s^s\right|}{\omega_{\bar{u}_s} L_m} \tag{50}$$

The value of (50) is applied during the first few sampling times and then it switches to the re-computation technique, as shown in Figure 9.

It can be concluded that the proposed rotor position estimator is independent of the variations in the stator voltage and stator frequency as well as the machine parameters. The only parameter that is present during the estimation is the stator leakage factor σ_s, which is a very small percentage of stator inductance L_s and it is not subjected to any saturation. Moreover, the estimated rotor position is calculated in terms of the unit vectors ($\sin\hat{\theta}_{me}$ and $\cos\ \hat{\theta}_{me}$) and not the inverse trigonometric function ($\tan^{-1}$), which suffers from discontinuity at definite operating times, which, as a result, deteriorates the estimation precision. Until now, all parts of the control system are designed, starting from Figure 8 passing through Figure 9, then the complete system configuration of the proposed sensor-less DPC for the DFIG can be constructed as shown in Figure 10.

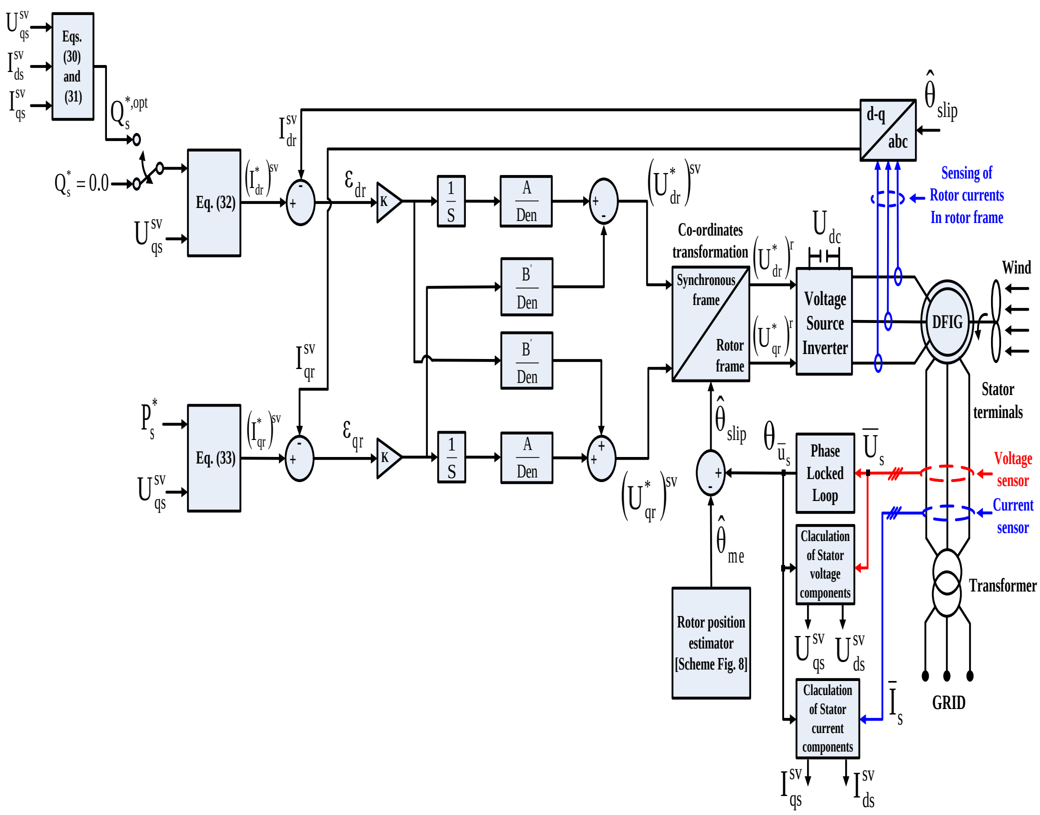

Figure 10. Complete system configuration for the proposed sensor-less direct power control (DPC) of DFIG.

4. Test Results

4.1. Testing Without LMC at Super-Synchronous Speed

To testify the feasibility of the proposed sensor-less DPC control approach for the DFIG, extensive simulation tests using Matlab/Simulink environment are carried out. The tests are carried out for two ranges of operating speed, the first when the rotor shaft is driven at the super synchronous speed (1.2 of synchronous speed), while the other when the rotor is driven at very low speed (nearly 1% of synchronous speed); this is to investigate the effectiveness of the sensor-less rotor position estimator at the specified operating speeds.

The tests start with applying a reference value of reactive power Q_s^* equal to zero to maintain the unity power factor condition. The active power reference P_s^* is set at starting with a value of 25 Kw and then increased at time t = 2.5 s to a value of 55 Kw. The rotor shaft is driven at the 1.2 times of the synchronous speed. The reference d-q current components I_{dr}^* and I_{qr}^* are derived using the relationships (32) and (33), respectively, to be used by the control system, as illustrated in Figure 10. The obtained results are shown in Figure 11, which illustrates the active power profile and through which the effectiveness of the proposed controller is investigated as the real power tracks precisely its reference. The same can be realized through Figure 12, in which the reactive power is maintained effectively at zero value. MoreoverFigures 13 and 14 show the profiles of d-q components of the rotor current, respectively. Through these figures, it can be seen that the d-axis I_{dr} tracks definitely its reference which is considered as a translation to the variation in the reactive power reference according to (32). While the q-axis I_{qr} follows the change in its reference with high matching degree, the latter is considered as a translation to the active power variation according to (33). Thus, the full decoupling has been achieved between the active and reactive power via utilizing the designed rotor current controllers.

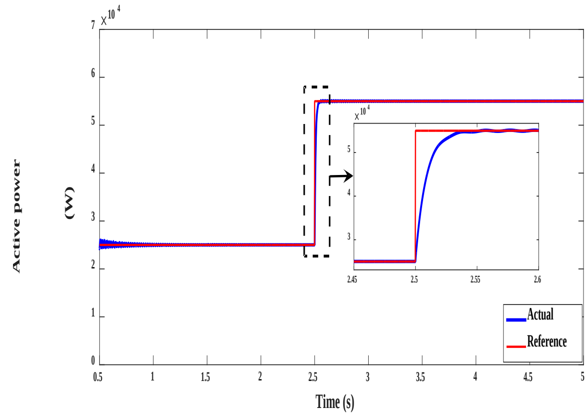

Figure 11. Active power (W).

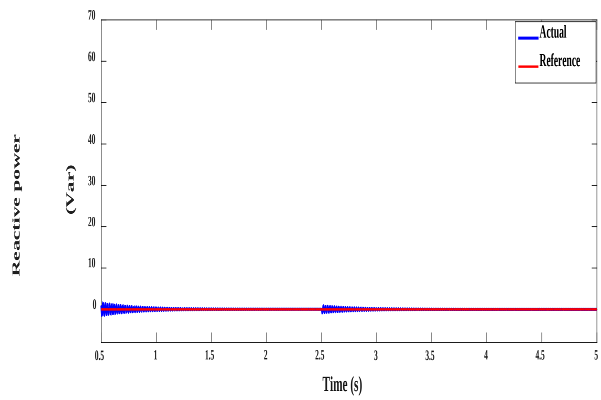

Figure 12. Reactive power (Var).

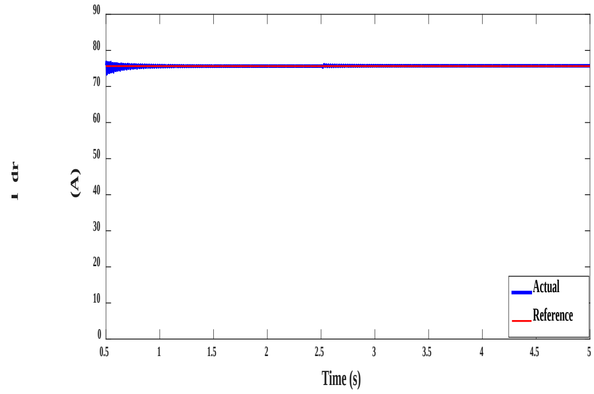

Figure 13. d-component of rotor current (A).

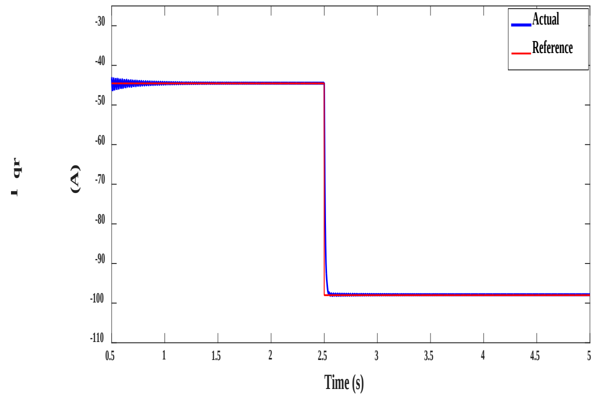

Figure 14. q-component of rotor current (A).

In Figure 15, the d-q components of the stator flux are shown, which confirm the validity of the proposed DPC in achieving the decoupling when adopting the stator voltage orientation (SVO), which specifies that the q-axis component is equal zero and the total stator flux is aligned to the direct axis. Figures 16 and 17 give the stator and rotor current profiles, which are used then to calculate the total power losses (iron+ copper) as shown in Figure 18. It is expected that the variation in Figure 18 should follow proportionally the variation in the active power.

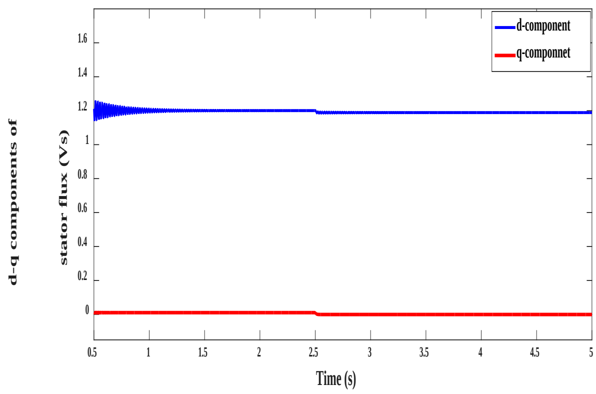

Figure 15. d-q components of stator flux (Vs).

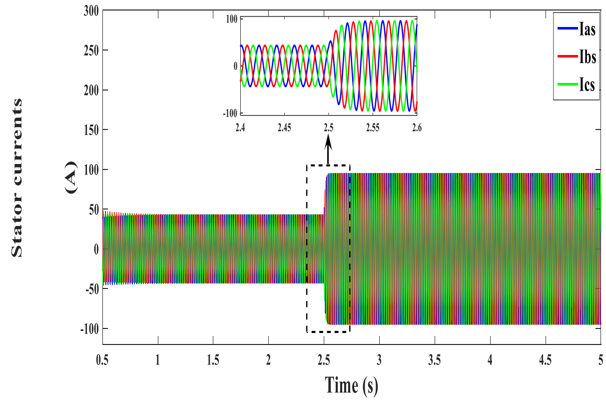

Figure 16. Stator currents (A).

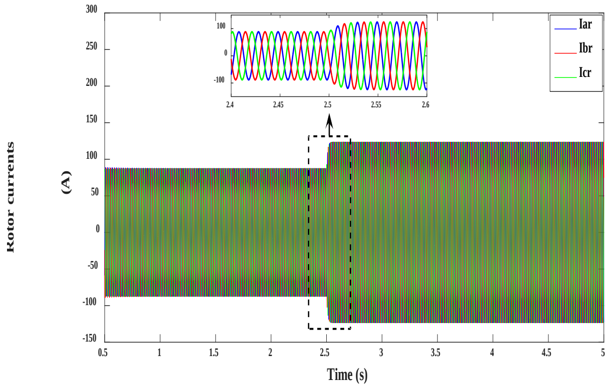

Figure 17. Rotor currents (A).

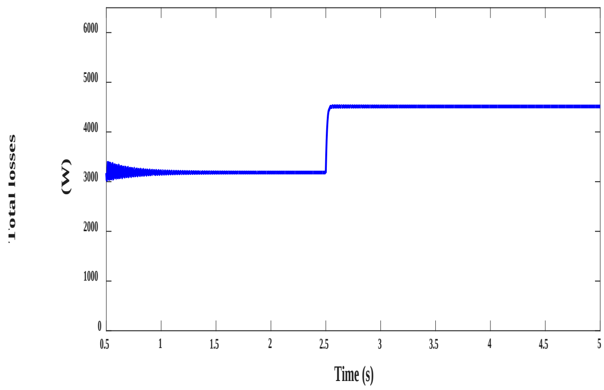

Figure 18. Total losses (W).

The most significant figures that outline the performance of the sensor-less rotor position estimator are shown in Figures 19 and 20, which illustrate the actual and estimated unit vectors of the rotor position $\sin\hat{\theta}_{me}$ and the error between them, respectively. A mismatch is made in the value of σ_s by 50% to check the robustness of the position estimator. In Figure 19, the effectiveness and precision of the estimator have been confirmed as the estimated values track precisely the actual values. Moreover, the calculated errors in Figure 20 are very small and can be neglected, which reconfirms the robustness of the estimator against the parameters' variation. The same thing can be noticed through Figures 21 and 22, which illustrate the actual and estimated values of the unit vector $\cos\hat{\theta}_{me}$ and the error between them, respectively. The obtained error values in Figure 22 assure the validity of the estimator.

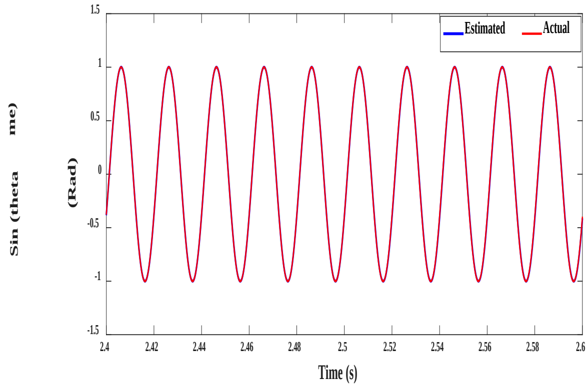

Figure 19. Actual and estimated sin $\hat{\theta}_{me}$ (Rad).

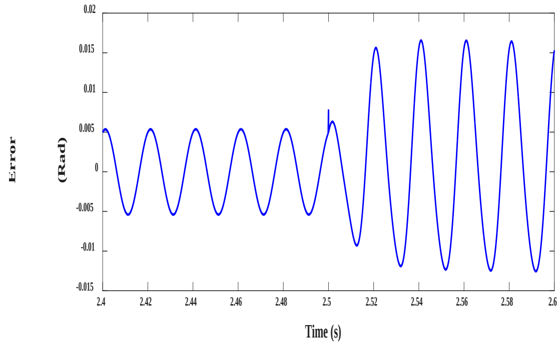

Figure 20. Error between actual and estimated sin $\hat{\theta}_{me}$ (Rad).

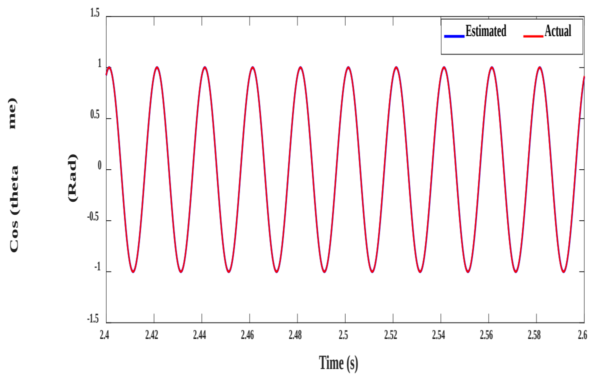

Figure 21. Actual and estimated cos $\hat{\theta}_{me}$ (Rad).

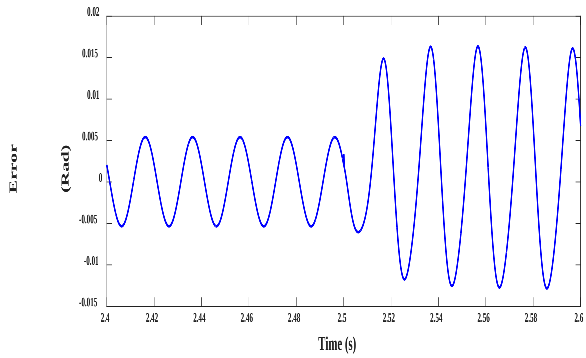

Figure 22. Error between actual and estimated cos $\hat{\theta}_{me}$ (Rad).

In addition, to introduce a focused view about the starting intervals of the estimation procedure, Figures 23 and 24 show the first instants of the estimation process, which reveals that the estimator does not take a long time to align the estimated position with its actual position, which confirms the validity of the position estimator when a mismatch in σ_s is present.

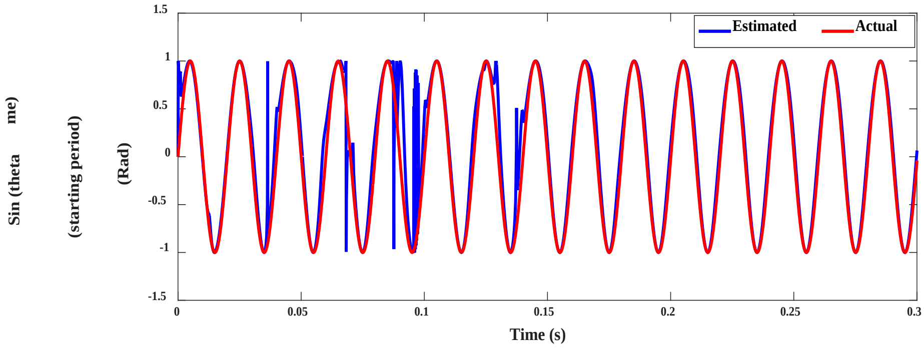

Figure 23. Actual and estimated $\sin\hat{\theta}_{me}$ at starting period(Rad).

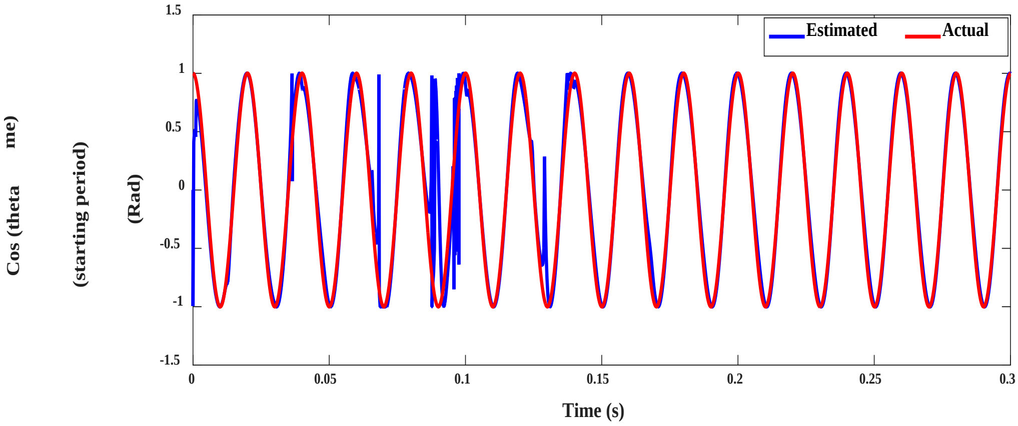

Figure 24. Actual and estimated $\cos\hat{\theta}_{me}$ at starting period(Rad).

4.2. *Testing with LMC at Super-Synchronous Speed*

The second test is carried out to validate the loss minimization criterion and show its effect on the losses minimization. The test is carried out for the same operating conditions of the previous test in which Q_s^* was set to zero. In the current test, the reactive power reference value (Q_s^*) is obtained using the formulation (32) to get $Q_s^{*,opt}$. The obtained results confirm the superiority of the LMC in limiting the DFIG total losses (iron+ copper) in comparison with previous test with constant Q_s^*. Moreover, the dynamic behavior of the DFIG presents high performance through achieving the decoupling between the active and reactive powers as shown in Figures 25 and 26, respectively. It can be noticed from Figure 26 that the reactive power exhibits a reduction at instant t = 2.5 s, and this is due to the reduction in the d-axis component of stator current which results from the increase in the d-axis component of rotor current I_{dr} as shown in Figure 27. The variation in the reactive power and I_{dr} can be investigated using the relationships (32) and (31), respectively. Figure 28 illustrates the behavior of the q-axis component of rotor current I_{qr}, which follows the variation in the active power according to the relationship (33). In Figure 29, the d-q components of stator flux are illustrated through which it can be concluded that the stator voltage orientation control is achieved by aligning the q-axis component to the null or zero value, while aligning the d-axis component to the total flux value.

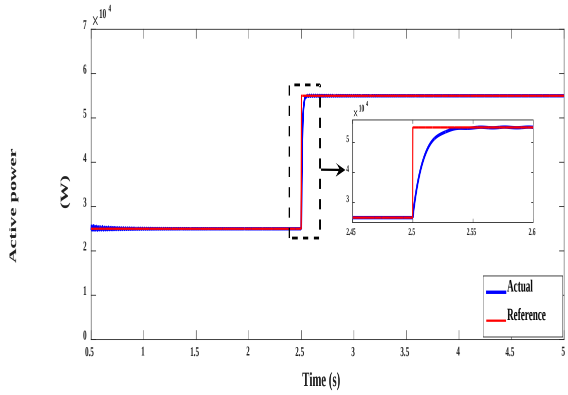

Figure 25. Active power (W).

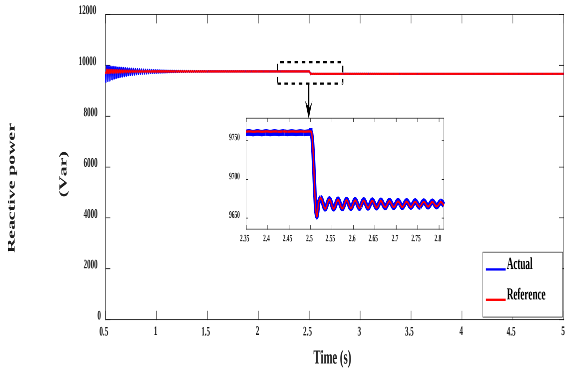

Figure 26. Reactive power (Var).

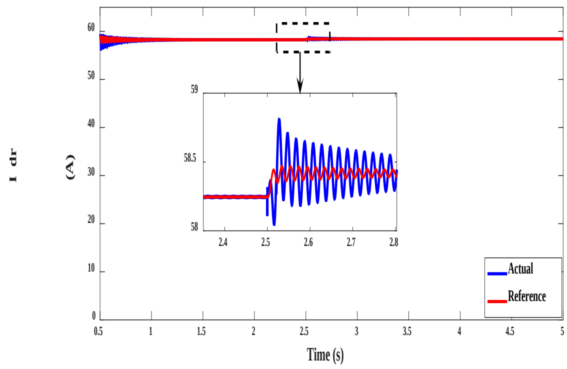

Figure 27. d-component of rotor current (A).

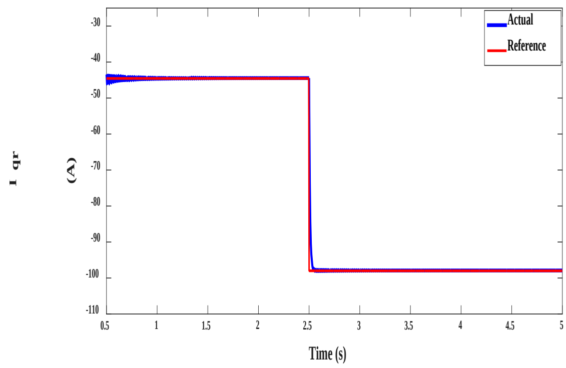

Figure 28. q-component of rotor current (A).

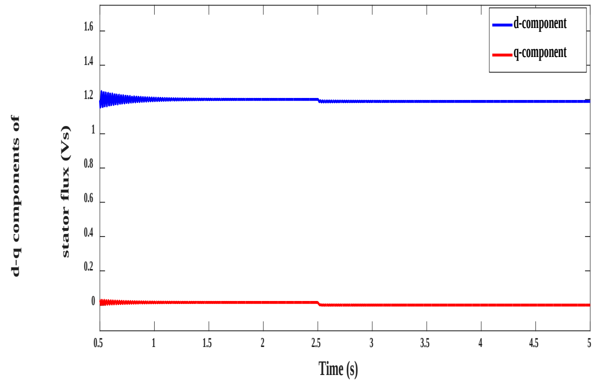

Figure 29. d-q components of stator flux (Vs).

The most significant effect of the LMC can be investigated through the current profiles. Figure 30 illustrates the stator currents waveforms, while Figure 31 shows the rotor currents profile through which it can be noticed that the rotor currents exhibit less values compared with the values in Figure 17, which confirms the effectiveness of the LMC in limiting the absorbed currents and thus limiting the losses. This can be investigated through Figure 32 which gives a comparison between the total losses for the two cases (without and with LMC), from which it is confirmed that the losses are effectively reduced using the LMC which improves the generation efficiency.

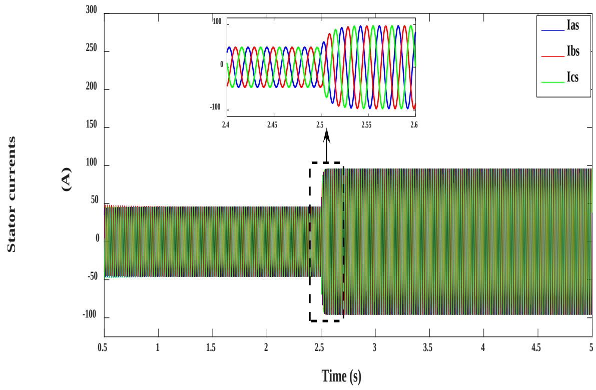

Figure 30. Stator currents (A).

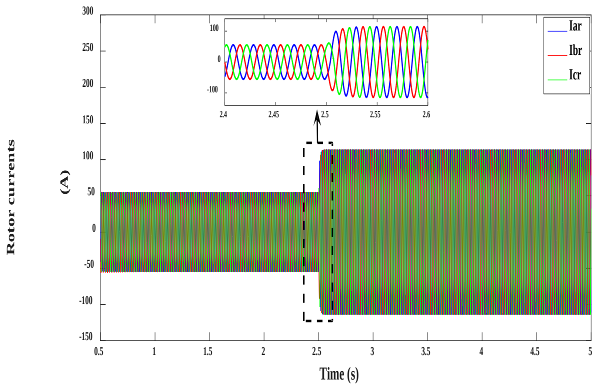

Figure 31. Rotor currents (A).

The unit vectors of the estimated rotor position $\sin\hat{\theta}_{me}$ and $\cos\hat{\theta}_{me}$ are illustrated with their corresponding errors in Figures 33–36, respectively. In Figure 33, the estimated unit vector '$\sin\hat{\theta}_{me}$' of the rotor position tracks precisely its actual value which makes the error almost null as shown in Figure 34 and which improves the co-ordinates transformation process. The estimator effectiveness is confirmed through checking Figures 35 and 36, which show the estimated and actual unit vector $\cos \hat{\theta}_{me}$ of the rotor position and its correspondence error, respectively. The calculated error values in Figure 36 are very small and can be neglected. All of these results are obtained under a mismatch in the stator leakage factor σ_s of 50%, which reveals the robustness of the observer against the system uncertainties. Finally, Figures 37 and 38 give a detailed view about the behavior of the estimator at a starting period until a complete match between the estimated and actual values is obtained.

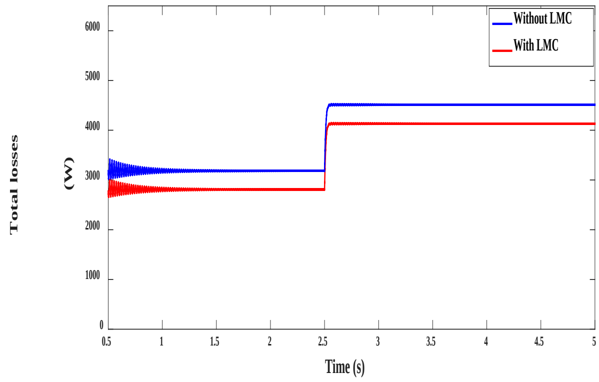

Figure 32. Total losses (W).

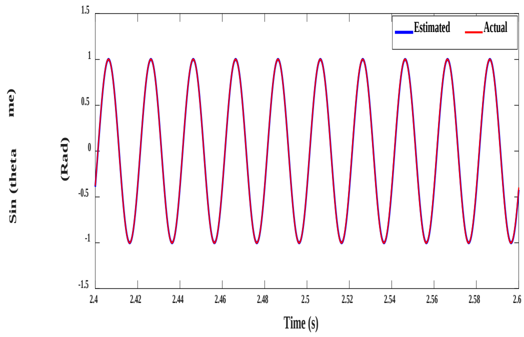

Figure 33. Actual and estimated $\sin \hat{\theta}_{me}$ (Rad).

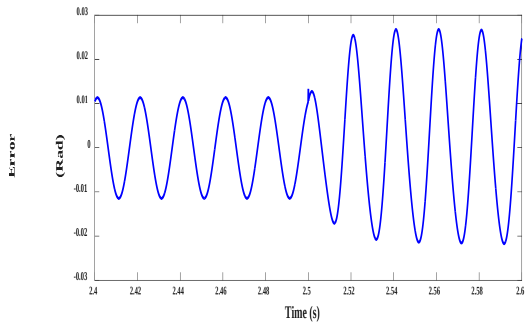

Figure 34. Error between actual and estimated $\sin \hat{\theta}_{me}$ (Rad).

4.3. Testing with LMC at Low Speed

The third test is carried out to investigate the performance of the sensor-less estimation procedure at low operating speeds (at 5 rad/s = 1% of synchronous speed). In this test, the reference value of the reactive power Q^* is applied using the LMC as in the second test. The reference value of the active power P^* is kept the same as in the previous two tests. The obtained results reconfirm the feasibility of the proposed sensor-less DPC for this operating range in achieving fast and accurate system response for the variations in the active and reactive powers. Moreover, the estimation of rotor position at very low speed is achieved with minimum estimation error.

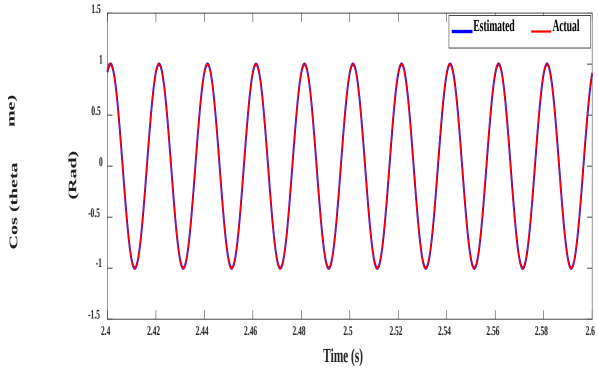

Figure 35. Actual and estimated cos $\hat{\theta}_{me}$ (Rad).

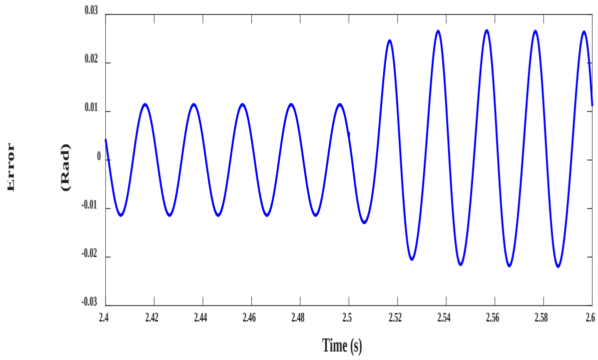

Figure 36. Error between actual and estimated cos $\hat{\theta}_{me}$ (Rad).

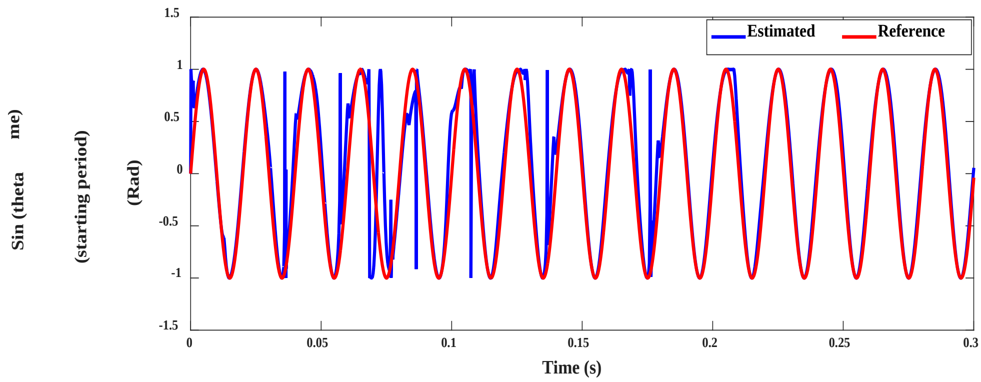

Figure 37. Actual and estimated sin $\hat{\theta}_{me}$ at starting period(Rad).

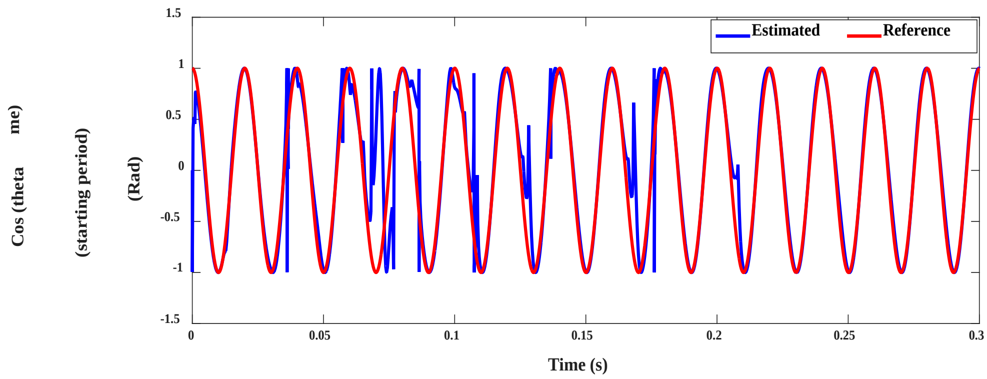

Figure 38. Actual and estimated cos $\hat{\theta}_{me}$ at starting period(Rad).

Figures 39 and 40 illustrate the active and reactive power profiles, which confirm the validity of the current controllers' design. Moreover, Figures 41 and 42 reveal the behaviors of the direct and quadrature axes of the rotor currents respecting to their references, respectively. The d-q components of the rotor current follow precisely their references, which initially follow the reactive and active powers' variation, respectively.

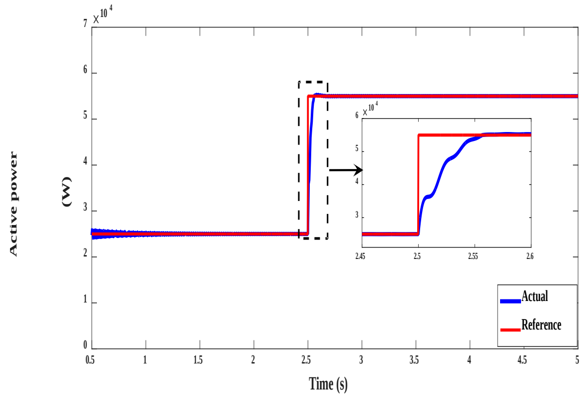

Figure 39. Active power (W).

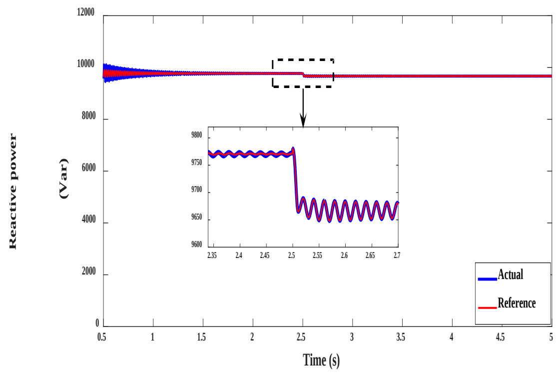

Figure 40. Reactive power (Var).

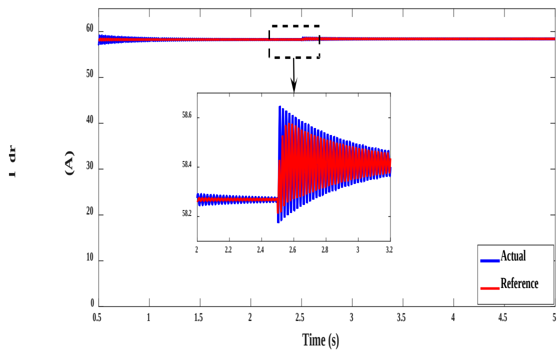

Figure 41. d-component of rotor current (A).

Full decoupling has been achieved between the direct and quadrature axes' components of the stator flux, and this can be viewed through Figure 43, which reveals that the correct stator voltage orientation is achieved via aligning the stator flux to the d-axis component and making the q-axis component equals zero.

The profiles of stator and rotor currents are illustrated in Figures 44 and 45, respectively. The rotor current profile shows a reduction compared with its profile in Figure 17, which confirms the validity of the LMC. The later action can also be investigated through Figure 46, which shows the total losses and presents a reduction compared with the losses in Figure 18.

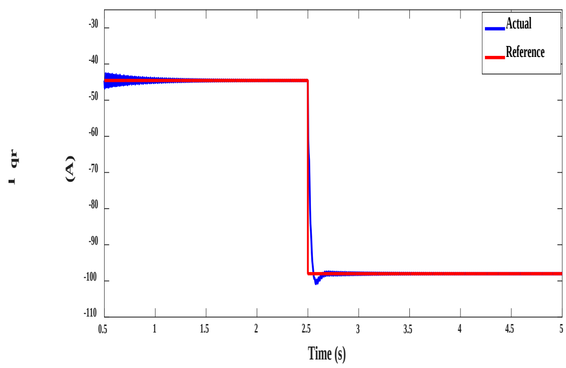

Figure 42. q-component of rotor current (A).

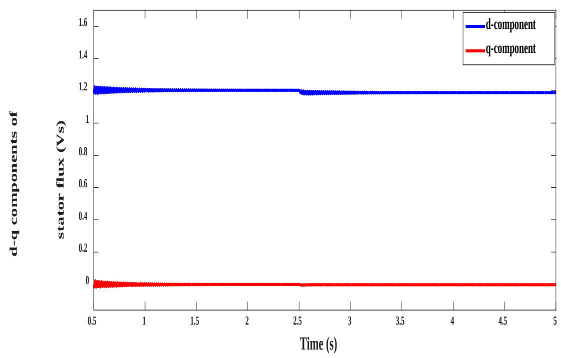

Figure 43. d-q components of stator flux (Vs).

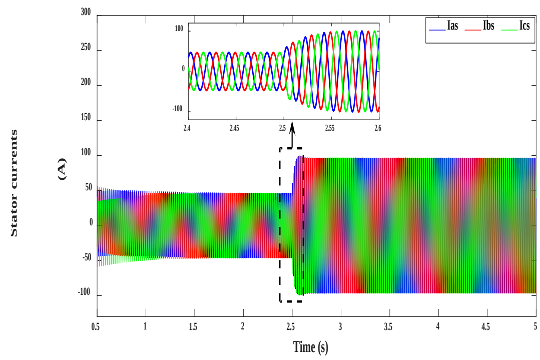

Figure 44. Stator currents (A).

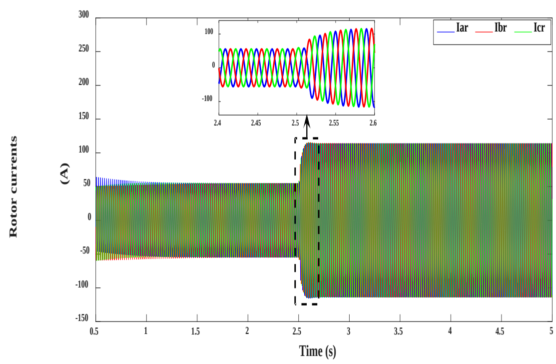

Figure 45. Rotor currents (A).

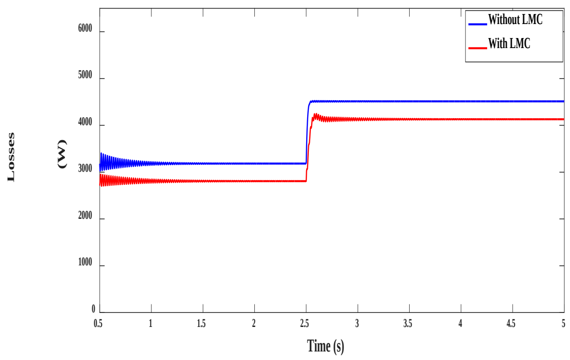

Figure 46. Total losses (W).

The most important figures that analyze the estimator performance are shown in Figures 47–50. These figures give the behaviors of the estimated unit vectors of the rotor position and their actual values. For example, Figure 47 shows the $\sin\hat{\theta}_{me}$ unit vector of the rotor position from which it can be realized that a precise estimation is achieved, while Figure 48 illustrates the error between the estimated and actual values, which gives null values and can be neglected. In the same manner, Figure 49 shows the estimated $\cos\hat{\theta}_{me}$ unit vector that tracks precisely its actual value, which makes the estimation error very small and can be ignored.

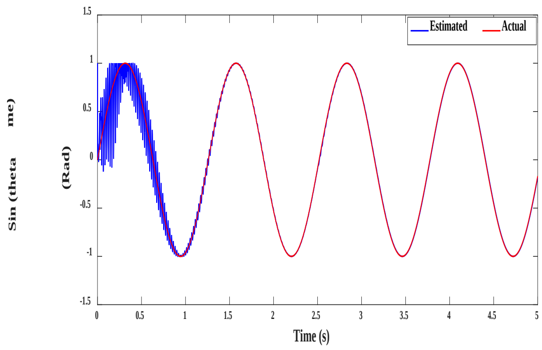

Figure 47. Actual and estimated $\sin\hat{\theta}_{me}$ (Rad).

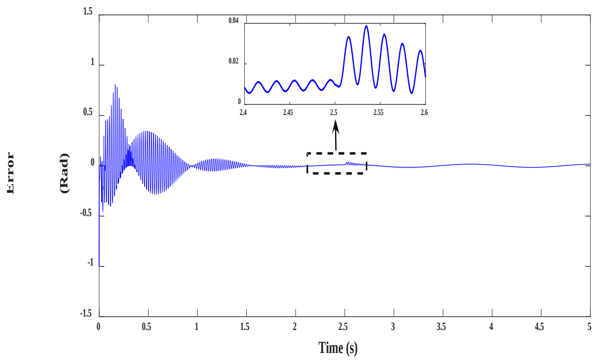

Figure 48. Error between actual and estimated $\sin\hat{\theta}_{me}$ (Rad).

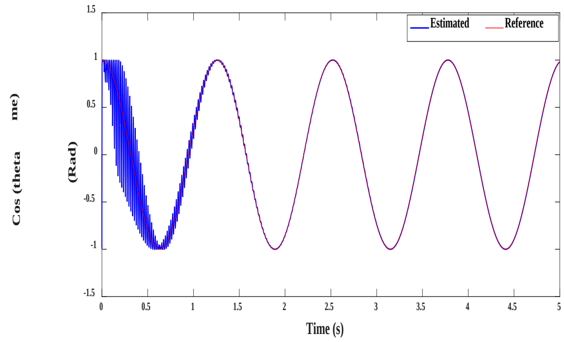

Figure 49. Actual and estimated cos $\hat{\theta}_{me}$ (Rad).

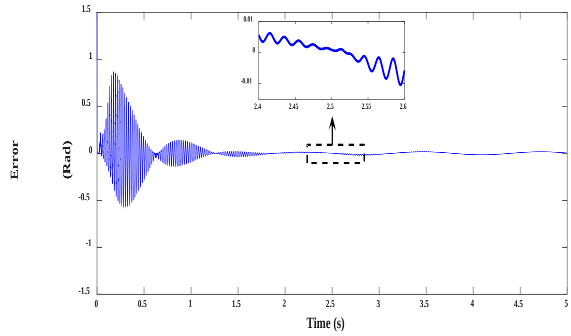

Figure 50. Error between actual and estimated cos $\hat{\theta}_{me}$ (Rad).

4.4. Evaluating the Performance of Previous Estimation Procedure

As stated earlier, the proposed rotor position estimator is robust against the parameters' variation, and this has been confirmed through estimating the rotor position for different operating speeds while changing the parameter (σ_s), which has an effect on the estimator. The obtained results confirm the high robustness of the estimator against the possible system uncertainties that prove the effectiveness of the proposed control methodology in comparison with some previous estimators that suffered from the sensitivity to the parameters' variation. To confirm the superiority of the proposed sensor-less procedure over a selected previous sensor-less scheme, the proposed DPC is tested when implementing the rotor position estimator presented in [46–48]. In these studies, the rotor position is extracted through determining the rotor current position in two different frames: the first is the position in the rotor frame, which is directly obtained through current measurement, while the other is the position of the rotor current vector in stationary frame, and this has been estimated through utilizing the machine voltage model and flux–current relationships as follows:

By defining the stator voltage equation in a stationary frame, the stator flux vector can be evaluated by:

$$\overline{\psi}_s^s = \int \left(\overline{u}_s^s - R_s \overline{i}_s^s\right) dt \tag{51}$$

Moreover, the stator flux vector can be represented in terms of stator and rotor currents as follows:

$$\overline{\psi}_s^s = L_s \overline{i}_s^s + L_m \overline{i}_r^s \tag{52}$$

Then, by substituting from (52) into (51), the rotor current vector $\overline{i}_r^s$ can be estimated in the stationary frame as follows:

$$\overline{i}_r^s = \frac{1}{L_m}\left[\int \left(\overline{u}_s^s - R_s \overline{i}_s^s\right) dt - L_s \overline{i}_s^s\right] \tag{53}$$

From Figure 2, to convert quantities between the stator and rotor frames, the rotor position (θ_{me}) is utilized, and this can be applied to the rotor current vector when transformed from the rotor to stator frame as follows:

$$\bar{i}_r^s = \bar{i}_r^r e^{j\theta_{me}} \tag{54}$$

where $\bar{i}_r^s$ and $\bar{i}_r^r$ are the rotor current vectors represented in stator and rotor frames, respectively.

The exponential in (54) can be expressed using the unit vectors. Then, from (53) and (54), it results:

$$\left(i_{dr}^r + j i_{qr}^r\right)(\cos\theta_{me} + j\sin\theta_{me}) = \frac{1}{L_m}\left[\int\left(\left(u_{ds}^s + j u_{qs}^s\right) - R_s\left(i_{ds}^s + j i_{qs}^s\right)\right)dt - L_s\left(i_{ds}^s + j i_{qs}^s\right)\right] \tag{55}$$

The only unknown variables in (55) are the position unit vectors ($\sin\theta_{me}$ and $\cos\theta_{me}$); then, by separating the d and q components in (55), we get:

$$\begin{aligned} i_{dr}^r\cos\theta_{me} - i_{qr}^r\sin\theta_{me} &= \overbrace{\frac{1}{L_m}\left[\int\left(u_{ds}^s - R_s i_{ds}^s\right)dt - L_s i_{ds}^s\right]}^{A} \\ i_{qr}^r\cos\theta_{me} + i_{dr}^r\sin\theta_{me} &= \overbrace{\frac{1}{L_m}\left[\int\left(u_{qs}^s - R_s i_{qs}^s\right)dt - L_s i_{qs}^s\right]}^{B} \end{aligned} \tag{56}$$

After some derivations, the unit vectors of rotor position can be expressed by:

$$\sin\theta_{me} = \frac{B i_{dr}^r - A i_{qr}^r}{\left|\, i_r^r \right|^2}, \text{ and } \cos\theta_{me} = \frac{A i_{dr}^r + B i_{qr}^r}{\left|\bar{i}_r^r\right|^2} \tag{57}$$

Then, it is conclude that the estimated unit vectors in (5) are depending on the machine parameters (mainly R_s, L_s and L_m) and this makes the estimator very sensitive to any variation in these quantities. To investigate this, the previous tests, which are performed using the new proposed estimator are also carried out using the estimator described by the relationships from (51) to (57) and which were implemented in several studies in the literature [46–48]. The test results show that the estimation process is drastically affected by the parameters' variation, which confirms the superiority of the proposed new estimator against the previous method. The test results for the old estimation technique are shown as follows:

4.4.1. Testing at Super Synchronous Speed

With a Mismatch in Stator Resistance (R_s) of 50%.

In this test, the performance of the estimator modeled by (51) to (57) is tested when applying a variation in stator resistance at time t = 2.5 s while applying the same conditions in the previous tests. The DFIG is running at super synchronous speed. As shown in Figures 51 and 52, that varying the resistance affects the calculated value of the unit vectors ($\sin\theta_{me}$ and $\cos\theta_{me}$), which affects negatively the transformation between different frames.

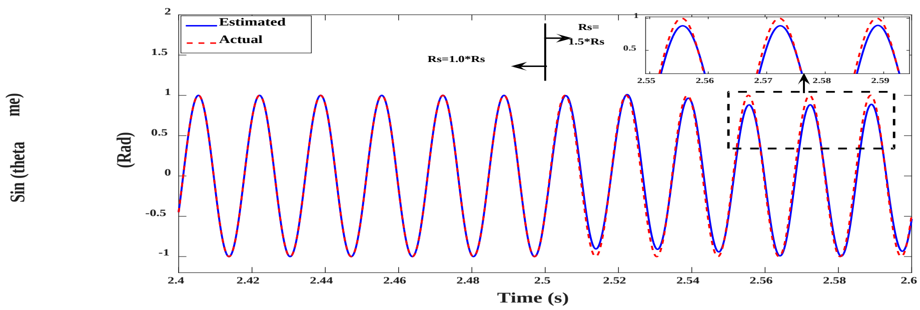

Figure 51. Actual and estimated $\sin\hat{\theta}_{me}$ under variation of R_s (Rad).

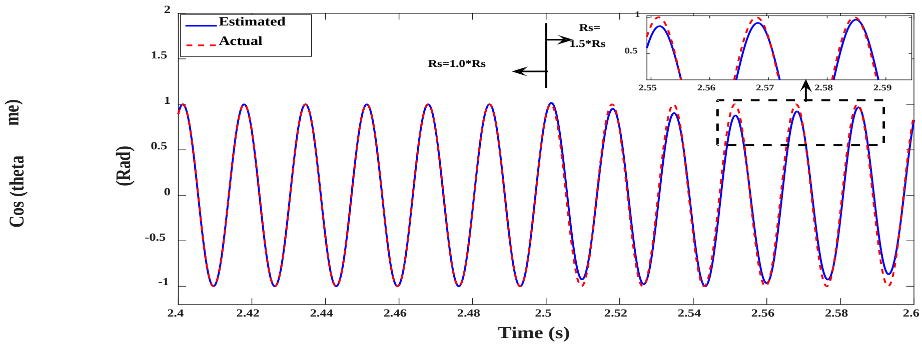

Figure 52. Actual and estimated cos $\hat{\theta}_{me}$ under variation of R_s (Rad).

With a Mismatch in Stator Inductance (L_s) of 5%.

A mismatch in the stator inductance (L_s) with 5% is applied at time t = 2.5 s. The results are shown in Figures 53 and 54, which illustrate that the estimated values of the unit vectors are affected by the applied variation.

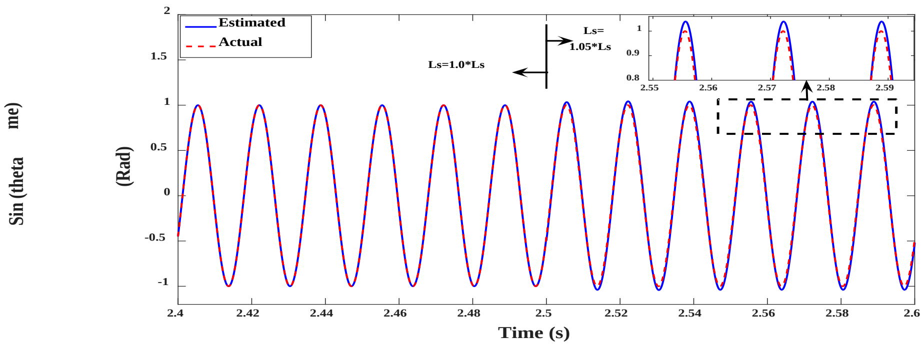

Figure 53. Actual and estimated sin $\hat{\theta}_{me}$ under variation of L_s (Rad).

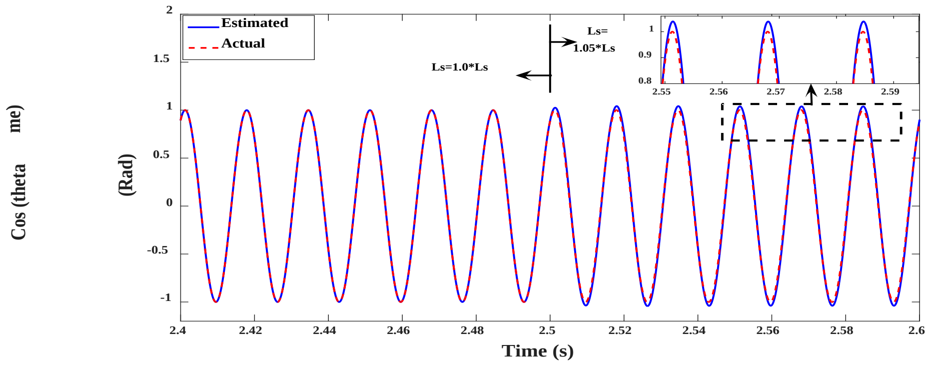

Figure 54. Actual and estimated cos $\hat{\theta}_{me}$ under variation of L_s (Rad).

With a mismatch in mutual inductance (L_m) of 10%.

A variation of 10% in the value of mutual inductance is applied at time t = 2.5 s. The results are shown in Figures 55 and 56, which illustrate the noticeable deviation between the estimated and actual values of the unit vectors after applying the mismatch.

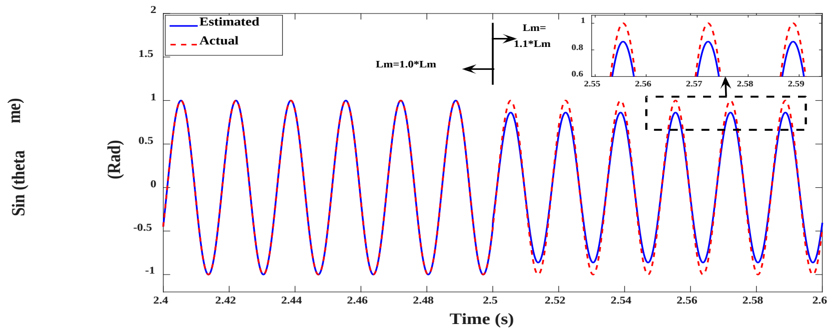

Figure 55. Actual and estimated sin $\hat{\theta}_{me}$ under variation of L_m (Rad).

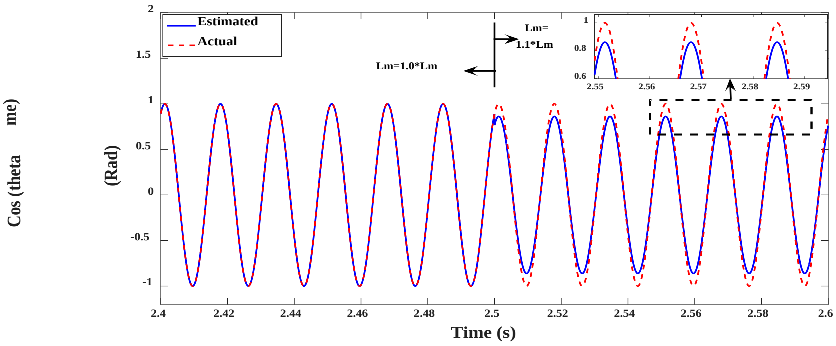

Figure 56. Actual and estimated cos $\hat{\theta}_{me}$ under variation of L_m (Rad).

4.4.2. Testing at Low Speed

With a Mismatch in Stator Resistance (R_s) of 50%.

The parameters' variation is also verified at a low-speed operation with the same operating power conditions in the previous tests. The obtained results show that the estimated unit vectors are negatively affected when a parameter mismatch is present. Figures 57 and 58 show the unit vectors profiles under a mismatch in R_s of 50%.

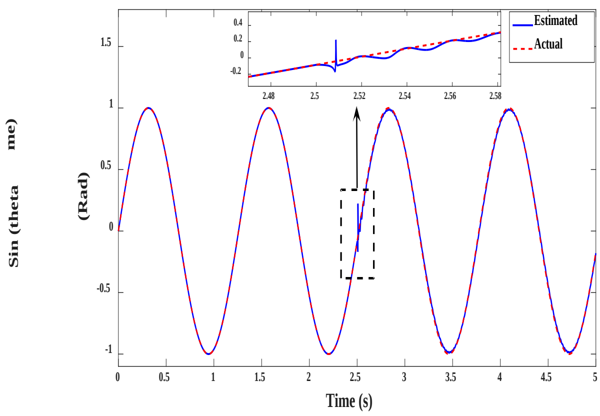

Figure 57. Actual and estimated sin $\hat{\theta}_{me}$ under variation of R_s (Rad).

With a Mismatch in Stator Inductance (L_s) of 5%.

A test has been carried out to show the response of the estimated signals to a variation of 5% in stator inductance. As illustrated in Figures 59 and 60, a deviation between the real and estimated unit vectors is noticed.

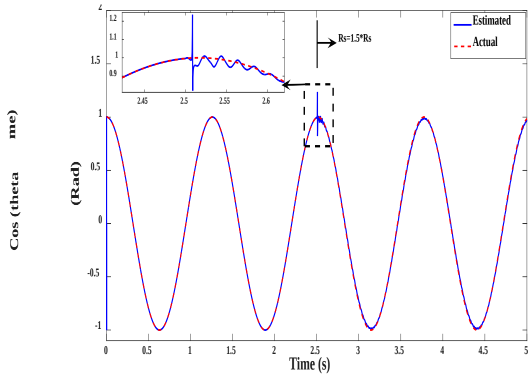

Figure 58. Actual and estimated cos $\hat{\theta}_{me}$ under variation of R_s (Rad).

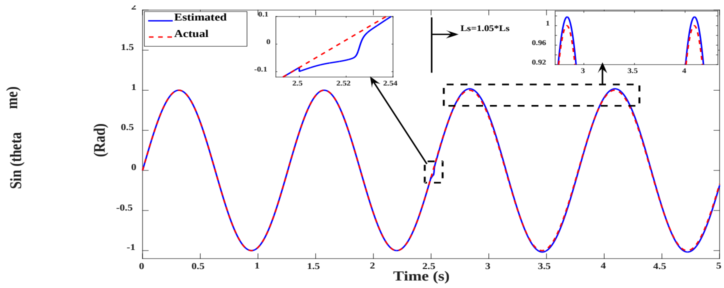

Figure 59. Actual and estimated sin $\hat{\theta}_{me}$ under variation of L_s (Rad).

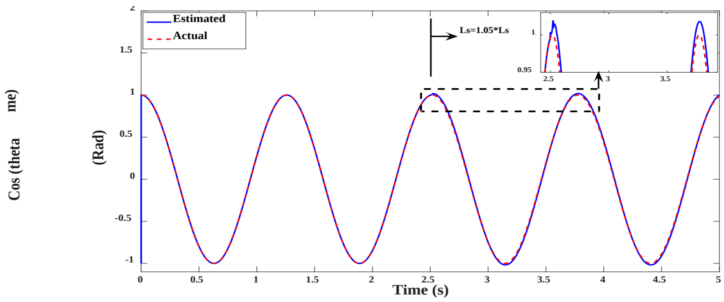

Figure 60. Actual and estimated cos $\hat{\theta}_{me}$ under variation of L_s (Rad).

With a Mismatch in Mutual Inductance (L_m) of 10%.

The last test for the low-speed operation is carried out when changing the value of mutual inductance to 1.1 times of its real value at time t = 2.5 s. The results are recorded in Figures 61 and 62, which show that the estimated signals make a shift with the actual quantities due to the effect of L_m variation.

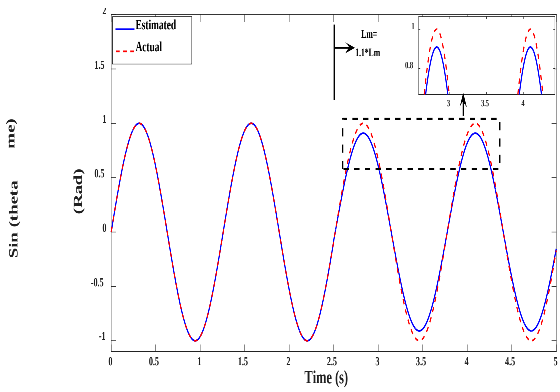

Figure 61. Actual and estimated sin $\hat{\theta}_{me}$ under variation of L_m (Rad).

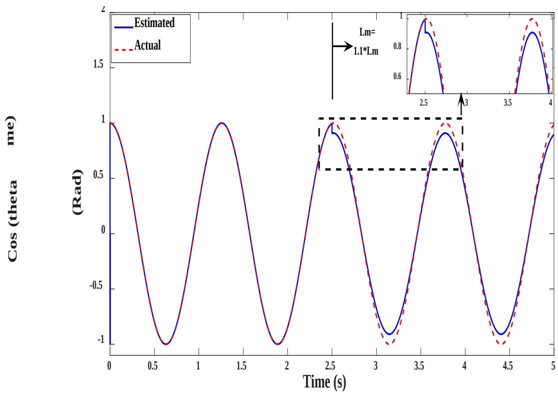

Figure 62. Actual and estimated cos $\hat{\theta}_{me}$ under variation of L_m (Rad).

From the previous tests, which are carried out to test the performance of the previous estimator, it can be concluded that the proposed estimator in the current paper has succeeded in avoiding the problem of the parameters' variation, which makes the proposed estimator very robust against the system uncertainties.

5. Conclusions

The paper has presented a robust sensor-less direct power control (DPC) approach for a doubly fed induction generator (DFIG). The design of the rotor current controllers is carried out in a systematic manner and illustrates the base principle of the proposed control approach, which makes the understanding of control steps easier. An effective losses minimization criterion (LMC) has been utilized to limit the iron and copper losses of the DFIG, which improves the generation efficiency. For enhancing the system robustness, an effective sensor-less procedure for estimating the rotor position has been proposed. The advantage of the proposed estimator is that it is independent of parameters variation compared with the previous estimation procedures. The feasibility of the proposed sensor-less DPC approach has been confirmed through carrying out extensive tests for a wide change in operating speeds, from a super-synchronous speed down to a very low speed (about 1% of the synchronous speed). The obtained results confirm and emphasize the robust performance of the rotor position estimator in estimating precisely the rotor position with minimal errors even under the parameters' variation. Moreover, the LMC has proved its capability in improving the generation efficiency of the DFIG.

Author Contributions: Conceptualization, M.A.M., H.E., A.A.Z.D.; methodology, M.A.M., N.V.Q and A.A.Z.D.; software, M.A.M., H.E. and N.V.Q.; validation, M.A.M. and H.E.; formal analysis, N.V.Q., M.A.M. and A.A.Z.D.; investigation, M.A.M., H.E. and A.A.Z.D.; resources, M.A.M. and H.E.; data curation, M.A.M. and N.V.Q.; writing—original draft preparation, M.A.M. and H.E.; writing—review and editing, M.A.M. and A.A.Z.D.; visualization, N.V.Q., A.A.Z.D. and H.E.; supervision, M.A.M. and N.V.Q.; project administration, M.A.M. and H.E.; funding acquisition, N.V.Q. All authors have read and agreed to the published version of the manuscript.

Funding: This work was supported by Lac Hong University.

Conflicts of Interest: The authors declare no conflict of interest.

Appendix A

Table A1. Parameters of DFIG and control system.

Parameters	Value	Parameters	Value
Rated power	55 kW	L_m	16 mH
R_s	70 mΩ	R_i	150 Ω
R_r	87 mΩ	U_{sn} (nominal stator voltage)	380 V
L_s	16.25 mH	U_{rn} (nominal rotor voltage)	365 V
L_r	16.3 mH	I_{sn} (nominal stator current)	115 A

References

1. Ma, J.; Zhao, D.; Yao, L.; Qian, M.; Yamashita, K.; Zhu, L. Analysis on application of a current-source based DFIG wind generator model. *CSEE J. Power Energy Syst.* **2018**, *4*, 352–361. [CrossRef]
2. Shu, Z.; Jirutitijaroen, P. Optimal Operation Strategy of Energy Storage System for Grid-Connected Wind Power Plants. *IEEE Trans. Sustain. Energy* **2014**, *5*, 190–199. [CrossRef]
3. Chen, Z.; Yin, M.; Zou, Y.; Meng, K.; Dong, Z. Maximum Wind Energy Extraction for Variable Speed Wind Turbines with Slow Dynamic Behavior. *IEEE Trans. Power Syst.* **2014**, *32*, 3321–3322. [CrossRef]
4. Almeida, R.G.D.; Castronuovo, E.D.; Lopes, J.A.P. Optimum generation control in wind parks when carrying out system operator requests. *IEEE Trans. Power Syst.* **2006**, *21*, 718–725. [CrossRef]
5. Tran, D.H.; Sareni, B.; Roboam, X.; Espanet, C. Integrated Optimal Design of a Passive Wind Turbine System: An Experimental Validation. *IEEE Trans. Sustain. Energy* **2010**, *1*, 48–56. [CrossRef]
6. Kalamen, L.; Rafajdus, P.; Sekerák, P.; Hrabovcová, V. A Novel Method of Magnetizing Inductance Investigation of Self-Excited Induction Generators. *IEEE Trans. Magn.* **2012**, *48*, 1657–1660. [CrossRef]
7. Joshi, D.; Sandhu, K.S.; Soni, M.K. Constant voltage constant frequency operation for a self-excited induction generator. *IEEE Trans. Energy Convers.* **2006**, *21*, 228–234. [CrossRef]
8. Chilipi, R.R.; Singh, B.; Murthy, S.S. Performance of a Self-Excited Induction Generator with DSTATCOM-DTC Drive-Based Voltage and Frequency Controller. *IEEE Trans. Energy Convers.* **2014**, *29*, 545–557. [CrossRef]
9. Guan, M.; Pan, W.; Zhang, J.; Hao, Q.; Cheng, J.; Zheng, X. Synchronous Generator Emulation Control Strategy for Voltage Source Converter (VSC) Stations. *IEEE Trans. Power Syst.* **2015**, *30*, 3093–3101. [CrossRef]
10. Haque, M.E.; Saw, Y.C.; Chowdhury, M.M. Advanced Control Scheme for an IPM Synchronous Generator-Based Gearless Variable Speed Wind Turbine. *IEEE Trans. Sustain. Energy* **2014**, *5*, 354–362. [CrossRef]
11. Hojabri, H.; Mokhtari, H.; Chang, L. Reactive Power Control of Permanent-Magnet Synchronous Wind Generator with Matrix Converter. *IEEE Trans. Power Deliv.* **2013**, *28*, 575–584. [CrossRef]
12. Cimino, M.; Pagilla, P.R. Reactive Power Control for Multiple Synchronous Generators Connected in Parallel. *IEEE Trans. Power Syst.* **2016**, *31*, 4371–4378. [CrossRef]
13. Nashed, M.N.F. Comparison between types of doubly fed induction generators converter with various switching techniques. *CIRED Open Access Proc. J.* **2017**, *2017*, 554–558. [CrossRef]
14. Duran, M.J.; Barrero, F.; Ruz, A.P.; Guzman, F.; Fernandez, J.; Guzman, H. Understanding Power Electronics and Electrical Machines in Multidisciplinary Wind Energy Conversion System Courses. *IEEE Trans. Educ.* **2013**, *56*, 174–182. [CrossRef]
15. Ong, C.M. *Dynamic Simulations of Electric Machinery: Using Matlab/Simulink*; Prentice Hall: Upper Saddle River, NJ, USA, 1998.
16. Lu, M.; Yin, W.; Peyton, A.; Qu, Z.; Meng, X.; Xie, Y.; Zhao, P.; Luo, J.; Zhao, Q.; Tao, Y.; et al. A model for the triboelectric nanogenerator with inductive load and its energy boost potential. *Nano Energy* **2019**, *63*, 103883. [CrossRef]
17. Yaramasu, V.; Wu, B.; Sen, P.C.; Kouro, S.; Narimani, M. High-power wind energy conversion systems: State-of-the-art and emerging technologies. *Proc. IEEE* **2015**, *103*, 740–788. [CrossRef]
18. Protsenko, K.; Xu, D. Modeling and Control of Brushless Doubly-Fed Induction Generators in Wind Energy Applications. *IEEE Trans. Power Electr.* **2008**, *23*, 1191–1197. [CrossRef]
19. Ekanayake, J.; Jenkins, N. Comparison of the response of doubly fed and fixed-speed induction generator wind turbines to changes in network frequency. *IEEE Trans. Energy Convers.* **2004**, *19*, 800–802. [CrossRef]
20. Alsmadi, Y.M.; Xu, L.; Blaabjerg, F.; Ortega, A.J.P.; Abdelaz, A.Y. Detailed Investigation and Performance Improvement of the Dynamic Behavior of Grid-Connected DFIG-Based Wind Turbines Under LVRT Conditions. *IEEE Trans. Ind. Appl.* **2018**, *54*, 4795–4812. [CrossRef]
21. Almeida, R.G.D.; Lopes, J.A.P. Participation of Doubly Fed Induction Wind Generators in System Frequency Regulation. *IEEE Trans. Power Syst.* **2007**, *22*, 944–950. [CrossRef]
22. Castilla, M.; Miret, J.; Matas, J.; Borrel, A.; Vicuna, L.G.D. Direct Rotor Current-Mode Control Improves the Transient Response of Doubly Fed Induction Generator-Based Wind Turbines. *IEEE Trans. Energy Convers.* **2010**, *25*, 722–731. [CrossRef]
23. Xiao, X.; Yang, R.; Zheng, Z.; Wang, Y. Cooperative Rotor-Side SMES and Transient Control for Improving the LVRT Capability of Grid-Connected DFIG-Based Wind Farm. *IEEE Trans. Appl. Supercond.* **2019**, *29*, 1–5.

24. Marques, G.D.; Sousa, D.M. Stator Flux Active Damping Methods for Field-Oriented Doubly Fed Induction Generator. *IEEE Trans. Energy Convers.* **2012**, *27*, 799–806. [CrossRef]
25. Marques, G.D.; Iacchetti, M.F. Stator Frequency Regulation in a Field-Oriented Controlled DFIG Connected to a DC Link. *IEEE Trans. Ind. Electr.* **2014**, *61*, 5930–5939. [CrossRef]
26. Abad, G.; Rodriguez, M.A.; Poza, J.; Canales, J.M. Direct Torque Control for Doubly Fed Induction Machine-Based Wind Turbines under Voltage Dips and Without Crowbar Protection. *IEEE Trans. Energy Convers.* **2010**, *25*, 586–588. [CrossRef]
27. Mondal, S.; Kastha, D. Improved Direct Torque and Reactive Power Control of a Matrix-Converter-Fed Grid-Connected Doubly Fed Induction Generator. *IEEE Trans. Ind. Electr.* **2015**, *62*, 7590–7598. [CrossRef]
28. Marques, G.D.; Iacchetti, M.F. DFIG Topologies for DC Networks: A Review on Control and Design Features. *IEEE Trans. Power Electr.* **2019**, *34*, 1299–1316. [CrossRef]
29. Wong, K.C.; Ho, S.L.; Cheng, K.W.E. Direct control algorithm for doubly fed induction generators in weak grids. *IET Electr. Power Appl.* **2009**, *3*, 371–380. [CrossRef]
30. Demirbas, S. Self-tuning fuzzy-PI-based current control algorithm for doubly fed induction generator. *IET Renew. Power Gener.* **2017**, *11*, 1714–1722. [CrossRef]
31. Jabr, H.M.; Lu, D.; Kar, N.C. Design and Implementation of Neuro-Fuzzy Vector Control for Wind-Driven Doubly-Fed Induction Generator. *IEEE Trans. Sustain. Energy* **2011**, *2*, 404–413.
32. Arbi, J.; Ghorbal, M.J.B.; Belkhodja, I.S.; Charaabi, L. Direct Virtual Torque Control for Doubly Fed Induction Generator Grid Connection. *IEEE Trans. Ind. Electr.* **2009**, *56*, 4163–4173. [CrossRef]
33. Martin, D.S.; Amenedo, J.L.R.; Arnalte, S. Dynamic Programming Power Control for Doubly Fed Induction Generators. *IEEE Trans. Power Electr.* **2008**, *23*, 2337–2345. [CrossRef]
34. Jovanovic, M.G.; Yu, J.; Levi, E. Encoderless direct torque controller for limited speed range applications of brushless doubly fed reluctance motors. *IEEE Trans. Ind. Appl.* **2006**, *42*, 712–722. [CrossRef]
35. Chen, S.Z.; Cheung, N.C.; Wong, K.C.; Wu, J. Integral variable structure direct torque control of doubly fed induction generator. *IET Renew. Power Gener.* **2011**, *5*, 18–25. [CrossRef]
36. Nian, H.; Song, Y. Direct Power Control of Doubly Fed Induction Generator under Distorted Grid Voltage. *IEEE Trans. Power Electr.* **2014**, *29*, 894–905. [CrossRef]
37. Martin, D.S.; Amenedo, J.L.R.; Arnalte, S. Direct Power Control Applied to Doubly Fed Induction Generator under Unbalanced Grid Voltage Conditions. *IEEE Trans. Power Electr.* **2008**, *23*, 2328–2336. [CrossRef]
38. Hu, J.; Zhu, J.; Dorrell, D.G. Predictive Direct Power Control of Doubly Fed Induction Generators under Unbalanced Grid Voltage Conditions for Power Quality Improvement. *IEEE Trans. Sustain. Energy* **2015**, *6*, 943–950. [CrossRef]
39. Rani, A.A.A.; Nagamani, C.; Ilango, G.S. Compensation of Magnetizing Current for Enhanced Operation of DFIG under Grid Unbalance. *IEEE Trans. Power Electr.* **2017**, *32*, 5214–5226. [CrossRef]
40. Pena, R.; Cardenas, R.; Proboste, J.; Asher, G.; Clare, J. Sensorless Control of Doubly-Fed Induction Generators Using a Rotor-Current-Based MRAS Observer. *IEEE Trans. Ind. Electr.* **2008**, *55*, 330–339. [CrossRef]
41. Cardenas, R.; Pena, R.; Asher, G.; Clare, J.; Cartes, J. MRAS observer for doubly fed induction Machines. *IEEE Trans. Energy Convers.* **2004**, *19*, 467–468. [CrossRef]
42. Susperregui, A.; Jugo, J.; Lizarraga, I.; Tapia, G. Automated control of doubly fed induction generator integrating sensorless parameter estimation and grid synchronization. *IET Renew. Power Gener.* **2014**, *8*, 76–89. [CrossRef]
43. Pattnaik, M.; Kastha, D. Adaptive Speed Observer for a Stand-Alone Doubly Fed Induction Generator Feeding Nonlinear and Unbalanced Loads. *IEEE Trans. Energy Convers.* **2013**, *27*, 1018–1026. [CrossRef]
44. Yu, S.; Fernando, T.; Iu, H.H.C.; Emami, K. Realization of State-Estimation-Based DFIG Wind Turbine Control Design in Hybrid Power Systems Using Stochastic Filtering Approaches. *IEEE Trans. Ind. Inf.* **2016**, *12*, 1084–1092. [CrossRef]
45. Chibah, A.; Menna, M.; Yazid, K.; Boufertella, A.; Djadi, H.; Boudour, M. Experimental design of a new fast sensorless control of DFIG in complex domain. *IET Electric Power Appl.* **2019**, *13*, 581–593. [CrossRef]
46. Morel, L.; Godfroid, H.; Mirzaian, A.; Kauffmann, J.M. Double-fed induction machine: Converter optimisation and field oriented control without position sensor. *IEE Proc. Electr. Power Appl.* **1998**, *145*, 360–368. [CrossRef]
47. Poddar, G.; Ranganathan, V.T. Sensorless field-oriented control for double-inverter-fed wound-rotor induction motor drive. *IEEE Trans. Ind. Electr.* **2004**, *51*, 1089–1096. [CrossRef]

48. Datta, R. Rotor Side Control of Grid-Connected Wound Rotor Induction Machine and Its Application to Wind Power Generation. Ph.D. Thesis, India Institute of Science, Bangalore, India, February 2000.
49. Wee, S.D.; Shin, M.H.; Hyun, D.S. Stator-flux-oriented control of induction motor considering iron loss. *IEEE Trans. Ind. Electr.* **2001**, *48*, 602–608.